Cement and Concrete Research 186 (2024) 107694

Contents lists available at ScienceDirect

Cement and Concrete Research

journal homepage: www.elsevier.com/locate/cemconres

Setting reaction of a olivine-based Mg-phosphate cement

Davide Bernasconi [a,*], Alberto Viani [b], Lucie Zárybnická [c], Simone Bordignon [d], Jose R.A. Godinho [e], Alexey Maximenko [f], Cem Celikutku [d], Sadaf Fatima Jafri [d,g,h], Elisa Borfecchia [d], Quentin Wehrung [a], Roberto Gobetto [d], Alessandro Pavese [a]

[a] Earth Sciences Department, University of Turin, Turin 10125, Italy
[b] Department of Chemical and Geological Sciences, University of Modena and Reggio Emilia, Modena 41125, Italy
[c] Institute of Theoretical and Applied Mechanics of the Czech Academy of Sciences, Centre Telč, Czech Republic
[d] Chemistry Department, University of Turin, Turin 10125, Italy
[e] Helmholtz Zentrum-Dresden Rossendorf, Helmholtz Institute Freiberg for Resource Technology, Freiberg 09599, Germany
[f] SOLARIS National Synchrotron Radiation Centre Jagiellonian University, Kraków 30-392, Poland
[g] Nanostructured Interfaces and Surfaces (NIS) Interdepartmental Centre, University of Torino, Via Pietro Giuria 7, 10125 Torino, Italy
[h] Department of Physics, University of Karachi, 75270 Karachi, Pakistan

ARTICLE INFO

Keywords:
Phosphate cement
Magnesium cement
Olivine
Alternative binders

ABSTRACT

The cementitious properties of natural Mg-rich olivine when reacted with a phosphoric acid solution are investigated, as a function of acid concentration and liquid/solid mass ratio. The obtained cements are composed of residual olivine crystals and amorphous silica nanoparticles dispersed in a dense and compact newberyite ($MgHPO_4 \bullet 3H_2O$) matrix. The latter was mostly formed by packed micrometric tabular crystals, although evidence of the presence of a fraction of amorphous $MgHPO_4$ was also found. Water content in the raw mix was observed to play a pivotal role on the reaction pathway, either promoting porosity or hindering the crystallization of the products. Up to 57 % of olivine reactivity, whose dissolution was promoted by the curing temperature (60 °C) and low pH, was achieved. All in all, these results indicate that the industrial mineral olivine may serve a viable source of Mg for the production of phosphate cements.

1. Introduction

Alternative binders are gaining interest as one of the technological solutions aimed at minimizing the carbon footprint of Portland cement production [1,2]. Between them, the acid-base cements take a special place [3]. They are dominated by phosphate binders, in which weakly basic or amphoteric (hydr)oxides react with phosphoric acid (PA)/phosphate salt aqueous solutions to produce phosphate compounds through acid-base/hydrolysis reactions [4–7]. Phosphate binders are also referred to as "chemically-bonded phosphate ceramics" (CBPCs) because they provide materials with low porosity and high mechanical strength [3,4,8], in which crystalline hydrates of low solubility occur often in association with amorphous phases [9]. Some CBPCs, such as the ZnO-based dental cements, are long known [8], others, like the phosphate-based geopolymers (PBGs) made by metakaolin (calcinated kaolinite, $Al_2Si_2O_7$) have been object of intense research in recent years [10–12]. The CBPCs based on metal-oxides exhibited flash/rapid setting, which hampered their use for many applications [13]. Pre-treatment of the oxides at high temperature was thus considered necessary to reduce their reactivity and mitigate the rate of dissolution [4,13]. The dead-burned magnesia obtained in this way has been employed in magnesium phosphate cements (MPCs), which are mostly based on struvite ($MgNH_4PO_4 \cdot 6H_2O$) or K-struvite ($MgKPO_4 \cdot 6H_2O$), with the addition of appropriate retarders (e.g., boric acid) to further control the setting properties [13–15]. MPCs exhibit interesting properties, such as high early strength (compressive strength up to 28 MPa in 1 h and above 40 MPa in 3 h), excellent resistance to abrasion and frost, fire-proof behaviour and low drying shrinkage [16–18]. Notwithstanding, their diffusion is limited by the high cost of MgO calcination (above 1500 °C) [3,13,14]. Among the possible solutions, there is the exploitation of alternative sources of Mg.

In this work, the industrial mineral Mg-olivine is tested as precursor for MPC formation. Olivine is an abundant natural silicate exhibiting full miscibility for the solid solution between forsterite (Mg_2SiO_4) and fayalite (Fe_2SiO_4) [19]. Due to its crystal structure consisting of isolated SiO_4^{4-} units interconnected by octahedra occupied by Mg/Fe, olivine

* Corresponding author.
E-mail address: davide.bernasconi@unito.it (D. Bernasconi).

https://doi.org/10.1016/j.cemconres.2024.107694
Received 1 July 2024; Received in revised form 17 September 2024; Accepted 2 October 2024
Available online 10 October 2024

Table 1
Chemical composition and physical properties of the raw material. The uncertainties are in the order of 2–3 %.

	Chemical composition (wt%)								BET (m^2g^{-1})	D_{50} (μm)	D_{90} (μm)
	MgO	SiO_2	Fe_2O_3	Al_2O_3	NiO	Cr_2O_3	CaO	LOI			
Raw material	49.1	41.4	7.3	0.5	0.3	0.4	0.2	0.6	2.7	20.4	61.3

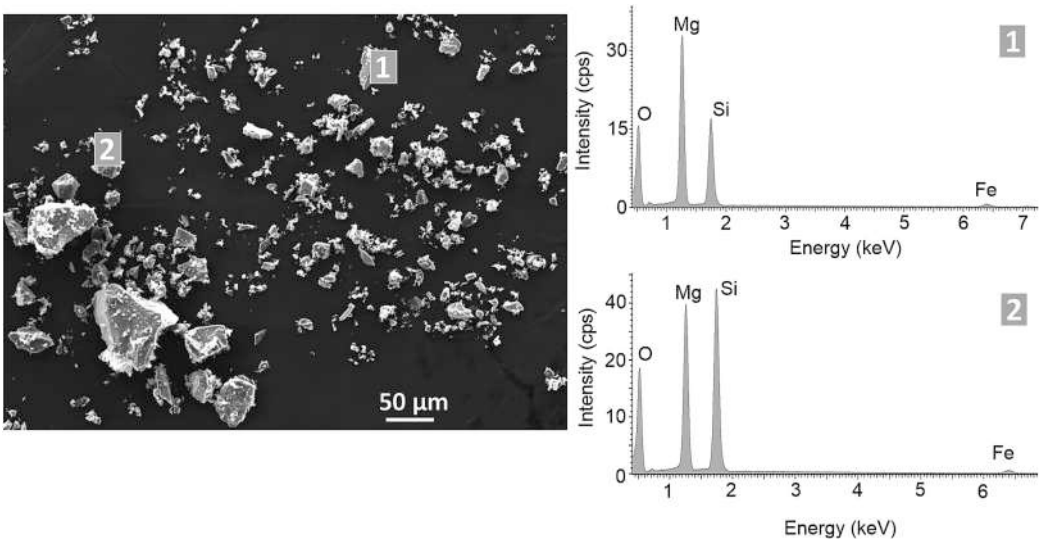

Fig. 1. SEM micrograph of milled raw material, together with EDS spectra of olivine (1) and enstatite (2).

possesses one of the highest dissolution rates among the silicate minerals, since the process requires only the breaking of the relatively weak Mg/Fe-O bonds [20]. This motivated its use to develop CO_2-mineralization strategies involving dissolution in acidic environments [20–22]. Olivine dissolution in strong sulphuric/hydrochloric acid has been also employed to synthesize high-purity MgO and nanosilica for cement-based materials [23,24].

The above experimental evidences suggest that the olivine dissolution in PA may provide a viable alternative to the reaction with magnesium oxide for the production of MPCs, similarly to what has been described for wollastonite ($CaSiO_3$) phosphate cements [9,25]. Further support comes from previous works on volcanic ash geopolymers, where a complex amorphous binding phase was observed to form when reacted with PA solutions. This was linked to the participation of the ash reactive phases (of which Fe-rich olivine is one of the components), that was reported to yield a Fe-Al-Mg-Ca phosphate gel [26–29].

For these reasons, the cementitious properties of olivine reacting with PA are here investigated as a function of acid concentration and liquid/solid mass ratio, by addressing molecular issues. The obtained cements were characterized in terms of mechanical properties, microstructure, reaction kinetics and structural features, adopting a combination of analytical techniques (compressive strength tests, isothermal conduction calorimetry (ICC), scanning electron microscopy coupled with energy dispersive spectroscopy (SEM-EDS), X-ray computed microtomographic (CT), X-ray powder diffraction (XRPD), thermogravimetric analysis-differential thermal analysis (TGA-DTA), ^{29}Si and ^{31}P solid-state NMR and synchrotron P K-edge X-ray absorption spectroscopy (XANES). Thermodynamic modelling has also been employed to help in the interpretation of the reaction mechanisms. We believe such results provide a significant contribution to understand this system and develop strategies for managing olivine-rich wastes (e.g., volcanic ashes, steel moulds, olivine sands), which can be employed in sustainable green processes to produce phosphate-based materials [26–30].

2. Materials and methods

2.1. Materials

The raw material employed in this study is the Norwegian olivine provided by Sibelco, reagent grade concentrated phosphoric acid (PA) solution (85 wt%, Sigma Aldrich, USA), ultrapure water. The olivine 90–180 μm fraction has been milled in the laboratory with a Mini-Mill Pulverisette 23 (Fritsch, Germany) at 40 oscillations/min for 8 min. Particle size analysis was performed in triplicate using a laser granulometer LD 1090 (Cilas, Orléans, France), and yielded an average particle size of d_{50} = 20 μm and d_{90} = 60 μm; the specific surface area was measured by the device ASAP 2020 (Micromeritics, Norcross, GA, USA) and resulted in 2.7 m^2/g (R = 0.9998). The bulk chemical composition of the raw material was determined by X-ray fluorescence on fused bead (Supermini Rigaku, Japan) and is reported in Table 1; a SEM-EDS micrograph of the milled particles is displayed in Fig. 1. EDS revealed the presence of minor amounts of enstatite ($(Mg,Fe)_2Si_2O_6$), whereas olivine occurred in a solid solution of Fo93-Fa7, $Mg_{1.86}Fe_{0.14}SiO_4$.

2.2. Formulation design

The formulation details of the investigated MPC pastes are reported in Table 2. A similar liquid-to-solid mass ratio (L/S) of 0.5, but different

Table 2
Formulations used for MPC samples. L/S: liquid-to-solid mass ratio; W/P: water/phosphorous molar ratio M/P: magnesium/phosphorous molar ratio.

	Raw material	PA	PA conc.	L/S	W/P	M/P
	g	*g*	*wt%*			
MPC1	10	5	60	0.5	3.6	4.0
MPC2	10	5	70	0.5	2.3	3.4
MPC3	10	5	80	0.5	1.4	3.0
MPC4	10	10	70	1.0	2.3	1.7

PA concentrations (60, 70 and 80 wt%) in the solutions were employed for MPC1, MPC2 and MPC3, respectively. In addition, a fourth sample (MPC4) was prepared with L/S set to 1.0 and a 70 wt% PA solution. These formulations allowed investigation about the role of the magnesium/phosphorus molar ratio (M/P) and of the amount of used water, expressed as water/phosphorous molar ratio (W/P), two parameters that are known to be pivotal in the definition of the MPCs reaction pathways [6,13].

The solutions were obtained by dilution from an 85 wt% PA solution. Powder and liquid were mixed with an automated mixer for 5 min; then the pastes were poured into silicone moulds, sealed in plastic bags and cured at 60 °C for as long as 24 h. This step was performed to accelerate the olivine dissolution [20]. After the curing stage, the samples were demoulded and left at room temperature for 1 month. Before the analyses, the samples were crushed and manually ground till a grain size <63 μm.

2.3. Analytical methods

The isothermal calorimetry experiment was conducted on the 4 studied formulations with a TAM-Air 8-channel instrument (TA Instruments, USA). For each sample the solution and the powder were loaded in the calorimeter using an Ad-Mix® ampoule, which allows keeping the two components separated. After they were equilibrated at the nominal temperature of the experiment (60 °C), the recording of the heat of the reaction started with the injection of the liquid onto the powder. The slurry was mixed for 30 s, and the heat flow was recorded for 24 h. Reproducibility was checked by measuring sample replicates.

The phase composition of olivine and hardened pastes was determined by XRPD measurements using a Rigaku SmartLab XE (Rigaku, Tokyo, Japan) diffractometer (Bragg-Brentano geometry, CuKα radiation, generator operating at 40 kV and 30 mA, divergence slit 0.33°, soller slits 2.5°) equipped with a two-dimensional semiconductor detector Hypix-3000. The energy resolution of the detector was increased to reduce the fluorescence signal from iron content in the raw material. XRPD patterns were collected from side-loaded samples between 5° and 70° 2θ, with a 2θ-step size of 0.02° and scan speed of 0.5°/min, while spinning at 60 rpm to reduce preferred orientation and texture effects. The Rietveld analysis, using high-purity corundum as an internal standard (10 wt%), was employed to determine the mineralogical composition of the raw material and cement pastes, including the amorphous content. The software Topas Academic V7 was adopted for the Rietveld refinement of XRPD patterns. The Rietveld strategy was based on the Fundamental Parameters approach and involved the refinement of 8 Chebyshev polynomial background coefficients, sample displacement parameter, phase scale and cell parameters, together with an isotropic (Lorentzian) crystallite size parameter of each phase. The site occupancy and database entries of the employed phases are listed in Table S1.

The refined phase fractions were used to calculate the dissolution degree (DD) of olivine in the samples, according to the formula:

$$DD = \left(1 - \frac{W_s(1+LS)}{W_i}\right) \times 100$$

where W_s and W_i represent the olivine phase fractions in the cement samples and raw material, respectively; LS is mass liquid-to-solid ratio in the formulation as set out in Table 2.

The thermal behaviour of the hardened cements was assessed by recording weight loss in the temperature range 30–750 °C using a STA 504 thermal analyser (TA Instruments, DE). The measurements were performed on powdered samples around 20 mg in weight at a heating rate of 20 °C/min under an N_2.

The SSNMR measurements on ^{31}P were recorded at room temperature on a solid-state NMR spectrometer (JNM-ECZR 600, JEOL RESONANCE Inc., Japan) with a magnetic field of 14.1 T, operating at ^{1}H and ^{31}P Larmor frequencies of 600.1 and 242.9 MHz, respectively. The ^{29}Si spectra were acquired with a Bruker Avance II 400 Ultra Shield instrument, operating at the ^{29}Si Larmor frequency of 79.5 MHz. The samples were packed into 3.2- and 4-mm zirconia rotors and spun at a MAS frequency of 20 and 12 kHz, for ^{31}P and ^{29}Si experiments, respectively. A 90° pulse of 5 μs, a relaxation delay of 50 s and a number of scans of 100 were set for ^{31}P single-pulse experiments, while a 90° pulse of 6 μs, a relaxation delay of 50 s and a number of scans of 1000 were employed for ^{29}Si single-pulse measurements. $^{31}P\{^{1}H\}$ cross-polarization spectra were collected with a contact time of 0.5 ms and relaxation delay of 1 s. ^{31}P chemical shifts scale was referenced through the resonances of external standard $(NH_4)H_2PO_4$ (^{31}P signal at 0.72 ppm with respect to 85 % H_3PO_4), while the ^{29}Si chemical shift scale was calibrated through the signal of external standard kaolinite (at −91.2 ppm with respect to TMS). The ^{29}Si chemical environments are expressed with the $Q^n(mAl)$ notation, where n indicates the number of the SiO_4^{4-} bridging oxygens and m indicates the number of Al to which they are connected to [31]. The SSNMR spectra deconvolution analysis was carried out using the Dmfit software [32], by employing pseudo-Voigt functions; the estimated uncertainty on the determined fractions is in the range of ±1 %.

The P K-edge XANES spectra of the samples were collected at the ASTRA Beamline of SOLARIS National Synchrotron Radiation Centre in Krakow (Poland). All the samples were finely ground, and thinly deposited on Kapton foil, to be measured in transmission mode. They were examined by using Ge (111) double crystal monochromator, at room temperature and in a N_2 atmosphere under low pressure of 11 Torr. A $FePO_4$ standard was measured for energy calibration to 2154.2 eV between samples. A number of scans ranging from 3 to 6 was collected for each sample, while the corresponding μ(E) curves were averaged after checking for signal reproducibility. The XAS spectra were collected with an energy step of 5 eV in the pre-edge region and of 0.2 eV in the near-edge region (XANES), with a time step of 1 s. The energy alignment and normalization to the edge-jump as well as XANES Linear Combination Fitting (LCF) analysis were performed by using the DEMETER open-source package (ATHENA) [33]. The reference spectra of two relevant magnesium-phosphate compounds, newberyite and bobierrite, and iron-phosphate compounds, namely strengite and vivianite, were retrieved from the inorganic P XANES database of the ESRF ID21 beamline [34–36].

Secondary electrons (SE) and back-scattered electrons (BSE)–EDS images were collected, and analyses performed, by a Tescan Vega scanning electron microscope equipped with a Ultim Max-15 EDS detector (Oxford Instruments), operating at 10 and 15 kV and beam current of 20 pA and 1 nA for imaging and chemical composition determination, respectively. EDS mapping was performed with Aztec software by employing a 512 × 386 grid, with a 0.1 μm pixel size and 0.3 ms dwell time. Additional maps on MPC4 sample were acquired on a Jeol JSM IT300 (JEOL USA Inc.) instrument equipped with a Ultim Max-65 EDS detector (Oxford Instruments) and operating at beam current and voltage of 4 nA and 15kV, respectively. The maps were collected with a 512 × 386 grid, having 0.1 um pixel size and 4 ms dwell time. The measurements were performed on samples retrieved from compression test fragment, either directly on exposed internal surfaces (morphology) or after epoxy-embedding and polishing (EDS maps). All the samples were C-coated before analysis.

X-ray computed micro-tomographic (CT) imaging of the MPC samples was performed at the Helmholtz Zentrum Dresden-Rossendorf in Freiberg (Germany), equipped with a CoreTOM (Tescan) scanner. Data were collected at room temperature on cylindrical samples (diameter of ~7 mm, height ~ 80 mm) at 140 kV and 15 W. The voxel size achieved with a detector binning of 2 was 8 um. 2142 2D radiographs (projections) with exposure time 1.6 s over a total angular range of 360°. A 0.155 mm stainless steel filter was used to mitigate beam hardening effect. The radiographs were reconstructed in three-dimensions (3D) with a filtered back-projection algorithm using the Panthera reconstruction software. The visualization of the reconstructed and filtered (anisotropic diffusion algorithm) two-dimensional (2D) slices was

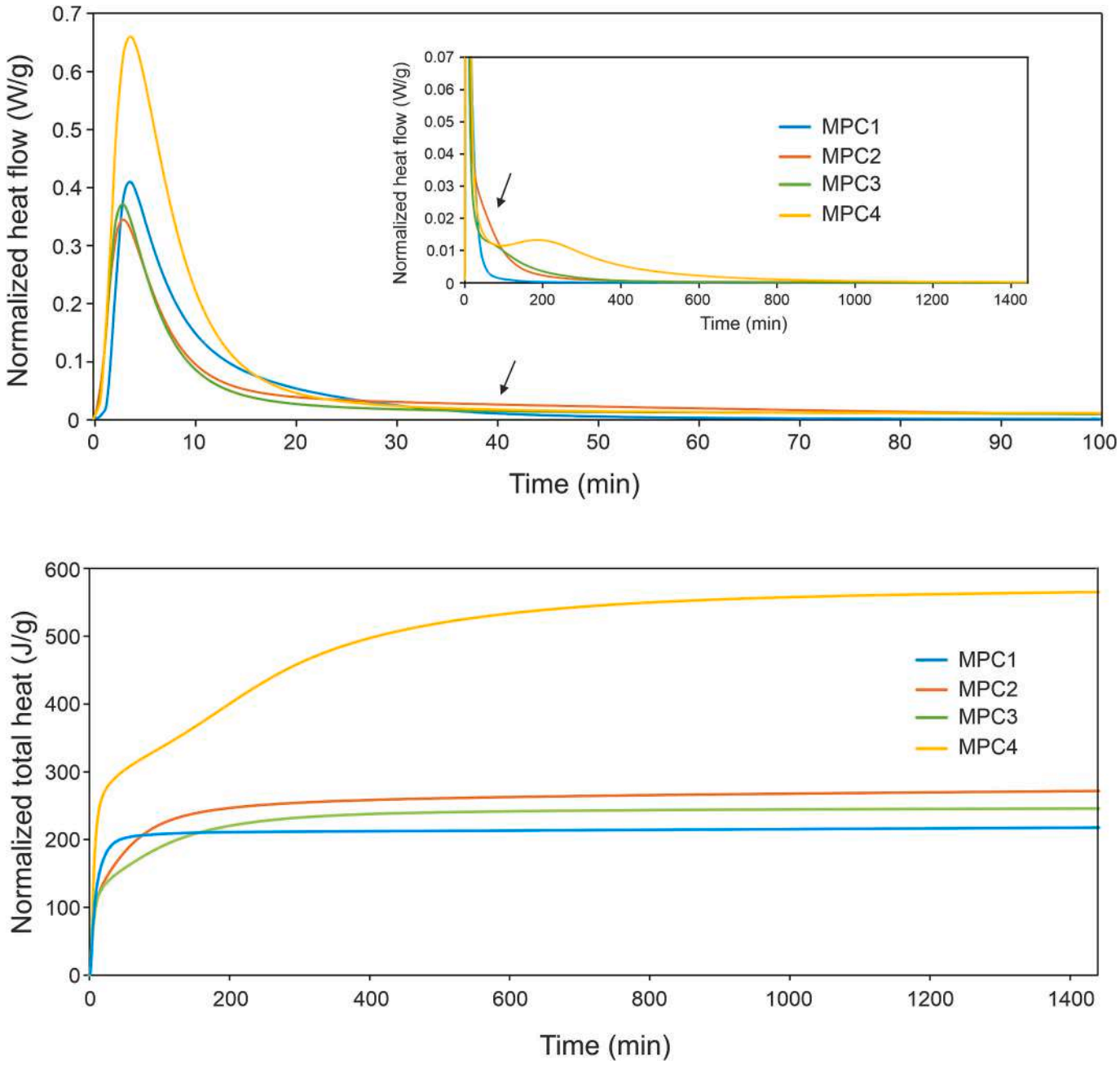

Fig. 2. Isothermal calorimetry curves collected at 60 °C. Top: heat flow normalized to the cement mass; bottom: cumulative total heat normalized to the cement mass. Arrows mark a contribution ascribed to product formation.

performed with the Fiji freeware software [37]. Subsequent segmentation, aimed at isolating microstructural features for the characterization and the quantitative image analysis, was accomplished with the software Dragonfly (ORS Inc., Canada) [38]. The selection of each grey level threshold was performed manually and kept constant between samples.

Compressive strength tests were performed on 30-day cured MPC cubes (1 × 1 × 1 cm), measuring 4 replicates by means of an Instron 3345 (Instron, USA) loading frame at a loading speed of 0.2 mm/min and 5 N load cell under laboratory conditions (23 ± 2 °C, room humidity 40 ± 5 %).

2.4. Thermodynamic modelling

The geochemical GEMS-PSI software [39], along with the PSI thermodynamic database [40], the cement-specific Cemdata18 [41] and the recently proposed database of magnesium phosphates magnesium silicate hydrates (M-S-H) [42,43], were used for simulations of the phase assemblages resulting from the olivine dissolution in the formulations of Table 1. GEMS was chosen as it directly models the Gibbs energy of the system and minimises it under the constraint of total bulk chemical composition [39,41]. Some assumptions were made in the definition of the model: i) enstatite was considered inert, since its kinetics of dissolution are significantly slower than those of forsterite; ii) Fo100 was used as a dummy of olivine (Fo93). Such approximations are motivated by the comparatively high purity of the employed raw materials and the lack of thermodynamic data on Fe-phosphates; iii) a fixed temperature of 60 °C was set, since the relative stability of magnesium phosphate phases is highly dependent on the temperature [37], although the samples were cured only for 24 h at 60 °C. The thermodynamic data at conditions of 1 bar but above 25 °C are calculated using the temperature

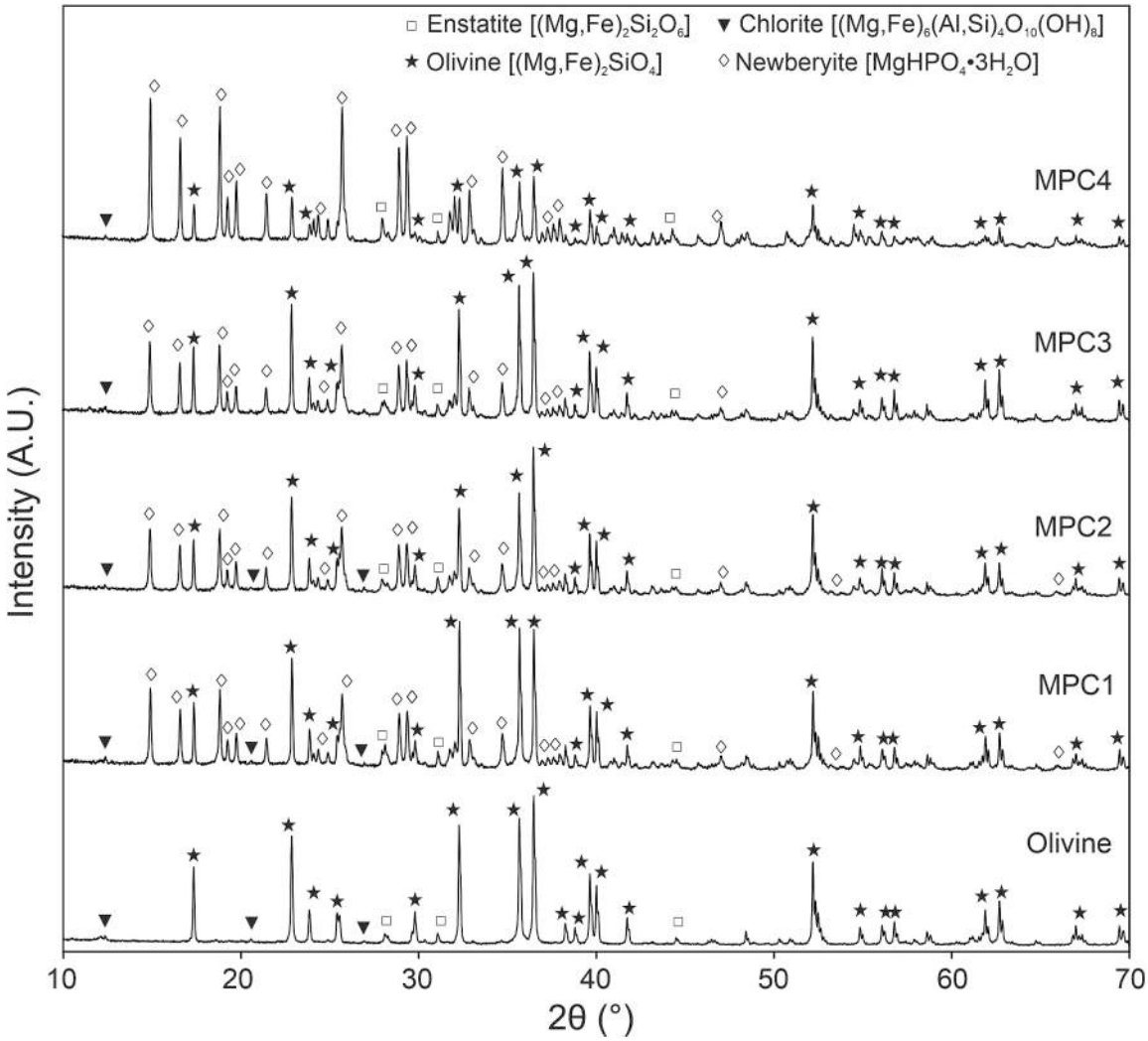

Fig. 3. X-ray diffraction patterns of olivine raw material and cement samples.

dependence of the "apparent" Gibbs free energy of formation as detailed below:

$$\Delta_a G^0_T = \Delta_f G^0_{T_0} - S^0_{T_0}(T - T_0) - \int_{T_0}^{T} dT' \int_{T_0}^{T'} \frac{C(T'')_P}{T''} dT'' = \Delta_f G^0_T - S^0_{T_0}(T - T_0) - a_0\left(T \ln\frac{T}{T_0} - T + T_0\right) - 0.5a_1(T - T_0)^1 - a_2\frac{(T - T_0)^2}{2TT_0} - a_3\frac{2\left(\sqrt{T} - \sqrt{T_0}\right)^2}{\sqrt{T_0}}$$

where a_0, a_1, a_2, and a_3 are the empirical coefficients of the heat capacity equation $C_p^0 = a_0 + a_1T + a_2T^{-2} + a_3T^{-0.5}$ and T_0 is the reference temperature (298.15 K). $\Delta_f G^0_{T_0}$ and $S^0_{T_0}$ refer to free energy and entropy of formation from the elements at 298 K, respectively. The above calculation is built into the GEMS-PSI code. A more detailed description of the derivation of the dependence of temperature of the Gibbs free energy is given in [39].

3. Results and discussion

3.1. Isocalorimetry

The recorded heat flow traces (normalized to the amount of cement) up to 100 min, collected at 60 °C to represent the curing conditions of the samples, are shown in Fig. 2 (top). All the curves are characterized by an intense exothermic peak appearing at the very beginning of the reaction and reaching its maximum within the first 10 min. MPC2 and MPC3 display similar peak positions and heights (2.8 min and 0.350–0.360 W/g, respectively), while MPC1 shows a slight delay and higher intensity (3.5 min and 0.401 W/g). MPC4 peaks to 0.650 W/g, at 3.6 min.

This first exothermic event is characterized by a marked asymmetry, which is more pronounced for MPC1, followed by MPC2, MPC3 and MPC4. When considering the full-time scale (inset in Fig. 2, top), it is apparent that a second component, evidenced by a change in slope, is present in all the heat flow curves (see arrows). The heat flow curve of MPC1 drops to negligible low values already after ~90 min, while for the other formulations this additional exothermic event is more resolved in time. In MPC4 it is clearly visible as a second maximum at around 200 min. When considering the curves of heat released after 24 h, illustrated

Table 3
Results of Rietveld quantitative phase analysis of the prepared samples. The reported errors represent the standard deviation of three different measurements at the same conditions.

	Raw material	MPC1	MPC2	MPC3	MPC4
	wt%				
Olivine	88.1 ± 1.1	43.9 ± 0.7	40.7 ± 0.6	39.2 ± 0.5	18.9 ± 0.6
Enstatite	8.7 ± 0.6	3.8 ± 0.5	4.1 ± 0.4	3.3 ± 0.4	2.6 ± 0.4
Chlorite	3.2 ± 0.2	2.1 ± 0.2	1.9 ± 0.2	1.9 ± 0.2	1.4 ± 0.2
Newberyite		31.9 ± 0.4	34.2 ± 0.5	20.1 ± 0.4	56.7 ± 0.6
Amorphous		18.2 ± 1.0	19.1 ± 0.9	35.0 ± 1.0	20.4 ± 1.1

in Fig. 2 (bottom), the MPC1 formulation, obtained with 60 wt% PA solution and the highest M/P ratio, confirmed its fast overall kinetics with the maximum of evolved heat reached already after 80–90 min. Moreover, this produced the lowest amount of heat (201.6 J/g) after 24 h.

In the formulation of MPC2, obtained by increasing the acid concentration (70 wt%), still preserving the same amount of liquid in the mix, the overall kinetics slow down. The isocalorimetric signal indicates that this should be mainly due to the contribution of the second event of heat release, forming a broad peak in the heat flow curve extended well beyond 300 min. This translates in an enhancement of the developed total heat after 24 h (270 J/g).

The increase in PA concentration (80 wt%) in MPC3 further extends the second enthalpic contribution in time. Here, the rates during the first reaction step are faster (higher heat flow peak at about 3 min) but they drop below those of MPC2 during the second reaction step. Therefore, the total released heat at 24 h takes intermediate values between MPC1 and MPC2 (240.6 J/g).

A different behaviour is exhibited by sample MPC4, which was formulated with the lowest M/P ratio but twice the amount of liquid with respect to the other samples. A remarkable increase in the overall rates with twice the amount of released heat is observed (524 J/g).

3.2. XRPD and TGA-DTG

The XRPD patterns of the olivine raw material and cement samples are displayed in Fig. 3. The results of the Rietveld quantitative phase analysis are reported in Table 3, while an example of the graphical output of a Rietveld refinement for MPC1 is illustrated in the Supplementary Material Fig. S1.

The raw material powder was composed of olivine (88 wt%), with minor amounts of enstatite and Mg-chlorite [44]. When turning to the cements, from a qualitative standpoint, it can be noticed that residual olivine remains in all the samples. This is a common aspect of this class of cements, since the powder dissolution step is frequently incomplete, owing to kinetic factors or an unfavorable stoichiometry with respect to some of the reagents (here M/P is significantly higher than 1) [5,6,13]. In all the diffraction patterns, peaks pertaining to newly formed newberyite ($MgHPO_4{\cdot}3H_2O$), were observed.

The quantitative phase analysis indicated that in the samples obtained by employing the same L/S ratio, the residual olivine content decreased down to around 40 wt%. This implies that around 25–33 % of olivine reacted, according to the concentration in the starting mixture (Table 2). Olivine dissolution increased with the decrease in M/P molar ratio. This is well exemplified in MPC4, where the higher amount of acid increased the olivine reactivity up to ~57 %, in agreement with the results of isothermal calorimetry (Fig. 2).

For most samples, the enhanced olivine dissolution correlated with the amount of precipitated newberyite (MPC4 > MPC2 > MPC1), whereas the amorphous fraction remained almost constant (18.2–20.4 wt%). At variance with this trend, in MPC3 the residual olivine was similar to that in MPC2, but the crystalline newberyite content dropped to its lowest value and the amorphous content achieved its maximum (35.0 wt%).

The TGA thermograms of cement samples are shown in Fig. 4, together with the related derivatives. For MPC1, MPC2 and MPC4, the main weight loss occurred between 140 and 250 °C. This is the

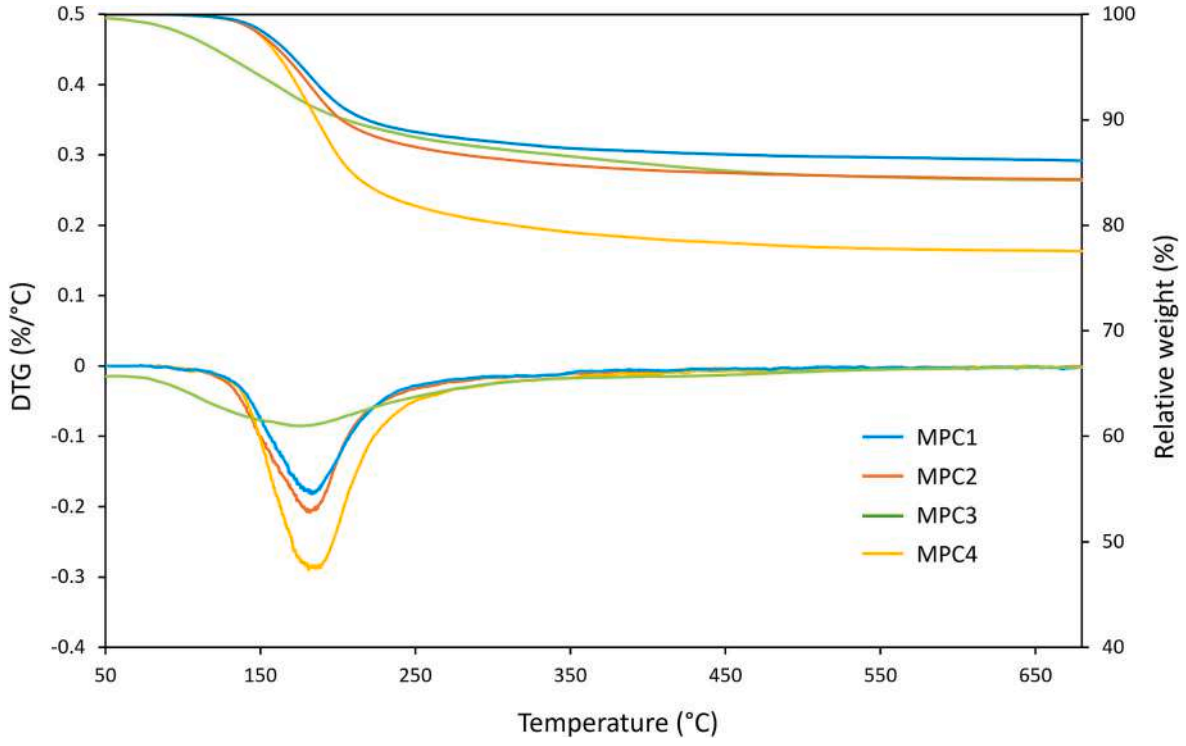

Fig. 4. Thermal analysis (TGA, top; DTG, bottom) of the MPC samples.

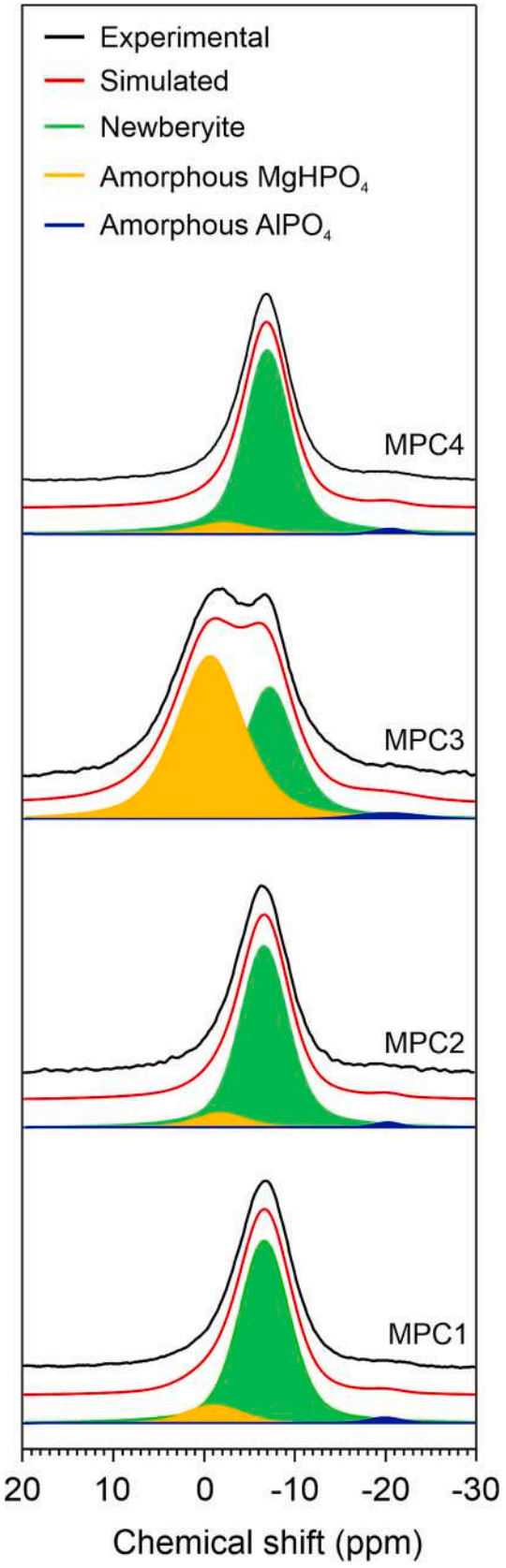

Fig. 5. ^{31}P MAS spectra of MPC samples (black lines), with deconvolution results (red lines) and assignments. Mg—P and Al—P stand for magnesium phosphate and aluminum phosphate, respectively. (For interpretation of the references to colour in this figure legend, the reader is referred to the web version of this article.)

temperature interval of the first step of thermal decomposition of newberyite, corresponding to its dehydration to obtain $MgHPO_4$ [45]. A further weight loss, up to 450–500 °C, is assigned to decomposition of the anhydrous $MgHPO_4$ into the corresponding pyrophosphate, $Mg_2P_2O_7$ [45]. According to the theoretical weight loss associated with newberyite (36 %) [40], a good match is observed with respect to the total measured weight loss and the one estimated through newberyite content by XRPD: 13.8 % and 11.5 % for MPC1; 14.9 % and 12.3 % for MPC2; 22.5 % and 20.4 % for MPC4. The measured difference (2.3, 2.6, 2.1 %, respectively) may be related to water bound to the X-ray amorphous phase. The thermogravimetric curve of MPC3 differed from those of the other samples since the weight loss started already at 40 °C, thus suggesting the presence of residual PA solution and dehydration of a hydrated gel, in accordance with the higher amorphous content detected by XRPD [26,27,46].

3.3. Spectroscopic analyses

3.3.1. Solid-state NMR

The single-pulse ^{31}P MAS spectra of the cement samples are presented as black lines in Fig. 5. All spectra displayed one peak centered at −7.1 ppm, assigned to the unique crystallographic P site of newberyite [47]. The broad lineshape, uncommon for crystalline compounds (Fig. 3) [31,48], was possibly related to the presence of paramagnetic elements (i.e., Fe), which are known to significantly broaden the NMR spectra due to the dipole-dipole interaction between nuclear and electron magnetic moments [49,50]. Moreover, a minor resonance centered at −19.5 ppm was identified, whose chemical shift could be assigned to amorphous aluminum phosphates formed by the partial dissolution of the chlorite impurities [11,12].

The spectra deconvolution allowed isolating an additional contribution, centred between −0.7 and − 1.5 ppm, whose resonance may be assigned to an amorphous HPO_4^{2-} component [47,51]. It is well evident in the MPC3 sample, where it comprises most of the signal (53 %, Table 4), although the different δ_{iso} (isotropic chemical shift) may indicate a variation in the local environment of phosphorus, as suggested by the TGA analysis. The results of ^{31}P{^{1}H} cross-polarization experiments, which enhance the signal from ^{31}P nuclei in close to hydrogen nuclei [52], are illustrated in Supplementary Material Fig. S2. In the MPC3 spectrum, the resonance assigned to the amorphous phase is visible, albeit less intense than the one pertaining to newberyite, indicating a less efficient magnetization transfer. This may be due to a lower concentration of protons, a larger distance between ^{1}H and ^{31}P nuclei, or a higher mobility (i.e. faster dynamics) [31,52]. Given its much lower intensity, we cannot prove/disprove the presence of this component in the MPC1, MPC2 and MPC4 samples, for which the signal was already very low in the single pulse ^{31}P MAS spectra.

The single-pulse ^{29}Si MAS spectra of the raw material and cement samples are presented in Fig. 6. The raw material spectrum was dominated by a very broad signal centered at −58.3 ppm, close to the chemical shift range of nesosilicates (Q^0), which is assigned to olivine [49,50]. Additional resonances at lower ppm values are related to the silicate impurities in the raw material, such as the inosilicate (Q^2) enstatite at −81.9 ppm and the phyllosilicate chlorite (Q^3(1Al)) at −93 ppm [53]. The anomalous broadening appears again in contrast with the high crystallinity of the raw material as determined by XRPD. Indeed, the paramagnetic broadening effects are markedly influenced by the interatomic distance between the paramagnetic ions and the target nuclei [50,54]. Two additional contributions were recognized, which correspond to the typical silanol (Q^3, −101 ppm) and bulk silicate (Q^4, −111 ppm) groups of amorphous silica [31,53].

Although the paramagnetic effects can negatively affect the accuracy of the quantification [31,53], the deconvolution results in Table 5 are in good agreement with those obtained from XRPD (Table 3). Along with the improved dissolution of olivine by increasing the concentration and amount of PA (26.8, 34.1, 35.9 and 60.8 % for MPC1, MPC2, MPC3 and

Table 4
Results of deconvolution of ^{31}P MAS spectra.

	MPC1		MPC2		MPC3		MPC4	
	δ_{iso}	Amount	δ_{iso}	Amount	δ_{iso}	Amount	δ_{iso}	Amount
	ppm	mol%	ppm	mol%	ppm	mol%	ppm	mol%
$MgHPO_4$ (am)	−1.5	8.7	−1.4	7.5	−0.7	52.9	−1.7	5.3
Newberyite	−7.1	89.8	−7.1	91.4	−7.1	44.9	−7.1	93.6
Al phosphate (am)	−19.2	1.5	−19.5	1.1	−19.4	2.2	−19.3	1.1

MPC4, respectively), a progressively larger fraction of produced silica was calculated.

3.3.2. P K-edge XANES

The P K-edge XANES spectra of the cement samples are presented in Fig. 7, along with reference spectra of two Mg phosphates, namely bobierrite ($Mg_3(PO_4)_2$•$8H_2O$) and newberyite, and two Fe-phosphate, such as strengite ($FePO_4$•$2H_2O$) and vivianite ($Fe_3(PO_4)_2$•$8H_2O$). The newberyite spectrum is characterized by an intense white line at 2152 eV, followed by a post-edge feature at 2156 eV and broad oscillations at 2165 and 2168 eV in the full multiple scattering regime. The bobierrite spectrum was characterized by a more structured signal, with a sharper oscillation at 2164 eV and a more extended post-edge feature at 2157 eV [34,55]. The strengite reference displayed a diagnostic pre-edge transition at 2148–2149 eV, assigned to the presence of Fe(III), while vivianite showed more evident post-edge features at 2156 and 2162 eV [35–36].

In the MPC samples, the spectral features of newberyite were observed without significant energy shifts (Fig. 7). On this basis, a linear combination fitting (LCF) has been attempted and the results are reported in the Supplementary Material Fig. S3. In all MPCs, newberyite accounted for >92 % of the signal, thus suggesting that the main local environment of P closely resembles that of a Mg hydrogen phosphate. This seems to be the case also for MPC3, which may provide support to the SSNMR assignment in Table 4. The reminder signal was tentatively assigned to bobierrite, although, in the LCF procedure, components occurring <10 mol% are usually considered below the quantification threshold [56,57]. Similarly, any attempt in introducing the Fe-phosphates spectra to the LCF resulted in a divergent or null contributions.

3.4. Microstructural investigations

3.4.1. SEM-EDS

The microstructure of the MPC samples is illustrated in the gallery of SEM micrographs in Fig. 8. The internal surfaces appeared rather compact, with unreacted olivine crystals embedded in a dense matrix. The newberyite crystals, recognized by EDS with an M/P ratio of 0.97–1.01 (Supplementary Material Fig. S4), thus close to the nominal values, were pervasive and densely packed. They were more developed inside some of the large pores, as shown by the micrographs of MPC4, where they exhibited a tabular pseudo-hexagonal habit, often accompanied by a hopper morphology, typical of fast crystallization [58]. The morphological analysis showed the presence of domains formed by the aggregation of micrometric and sub-micrometric particles. They impaired the compactness of the microstructure and appeared more developed in MPC1, as illustrated in the corresponding high-magnification micrograph in Fig. 8. An amorphous, or gel-like, phase exhibiting a different morphology is also observed in MPC3 (Fig. 8). The EDS spectra in Fig. S4 suggest that neither P-rich gel nor a magnesium phosphate phase are present.

The cement cross-sections investigated with BSE-EDS (Fig. 9) further confirmed these observations. The “aggregation” domains in MPC1 clearly evidenced a higher microporosity and were composed by micrometric particles of amorphous silica and some residual olivine crystals, in contrast with the other compact regions (lower right half of the micrograph), rich in Mg phosphate (i.e., newberyite) intermixed with precipitated silica, embedding the olivine grains. The EDS maps in Fig. 9 clearly showed that the amount of newberyite in these regions was higher in sample MPC4 than MPC1 and MPC2, in agreement with XRPD (Table 3). In MPC3, the amorphous phase (bottom right) was more abundant than in the other samples and displayed a chemical composition very similar to the one of the crystalline regions (top left), albeit enriched in P, with a mean M/P ratio of 0.92 (Supplementary Material Fig. S5). Additional EDS maps on MPC4 showed a relatively homogenous distribution of iron in the matrix, together with small regions rich in Mg-P-Fe, suggesting a preferential binding to the phosphates (Supplementary Material Fig. S6). From the microstructural point of view, the polished sections evidenced the presence of diffused microcracks, which may be due to the sample preparation procedure, although similar crack patterns have been previously reported in volcanic ash geopolymers as well as MPCs based on struvite or K-struvite and ascribed to dehydration and shrinkage effects during curing [26,28,59–61]. This suggests that control on curing process is fundamental to improve the mechanical performance of these materials [62].

3.4.2. CT

The MPCs microstructure has been further investigated by CT. Examples of slices of the reconstructed volumes are shown in Fig. 10. From a qualitative point of view, the cement samples appeared compact with the brighter olivine crystals homogeneously distributed throughout the phosphate matrix. A limited porosity was present, mostly due to subspherical pores, caused by air entrainment [63]. The MPC1 sample was characterized by extensive dendritic domains whose darker distribution of grey levels resulted from the association of a higher fine porosity and a low absorption (inset Fig. 10), in agreement with SEM-EDS observations (Fig. 8–9). In addition, in MPC2 the total porosity was also contributed by cracks, frequently starting from the subspherical pores and/or connecting them, that may be ascribed to drying shrinkage during the material hardening [64]. In fact, in brittle materials pores act as stress concentrators [65]. These cracks are present in the sample MPC3, although with lower density and size, while are not observable in the sample MPC4.

The quantitative image analysis has been performed by defining four classes of objects, according to their distribution of grey levels, namely: 1) voids (pores and cracks), with the lowest absorption; 2) the intermediate region as described above for MPC1; 3) the P-rich matrix; 4) the olivine and minor phases denser than olivine (light grey to white). The poor contrast between the amorphous phase and crystalline newberyite cannot allow one to obtain a reliable quantification. The adopted approach and an example of the definition of the thresholds for the volume segmentation are provided in Supplementary Material Fig. S7, while 3D renderings of cylindrical ROIs of the obtained segmented classes are shown in Fig. 11. The retrieved quantitative data are summarized in Table 6. It is worth mentioning that the spatial resolution limits the accuracy of the quantification of smallest/finer features; it is the case of a fraction of olivine crystals and intermediate phases. Nonetheless, since the same grey thresholds are employed for all the samples, the errors are expected to be similar, thus allowing for a relative comparison between the samples, even though the absolute volumes

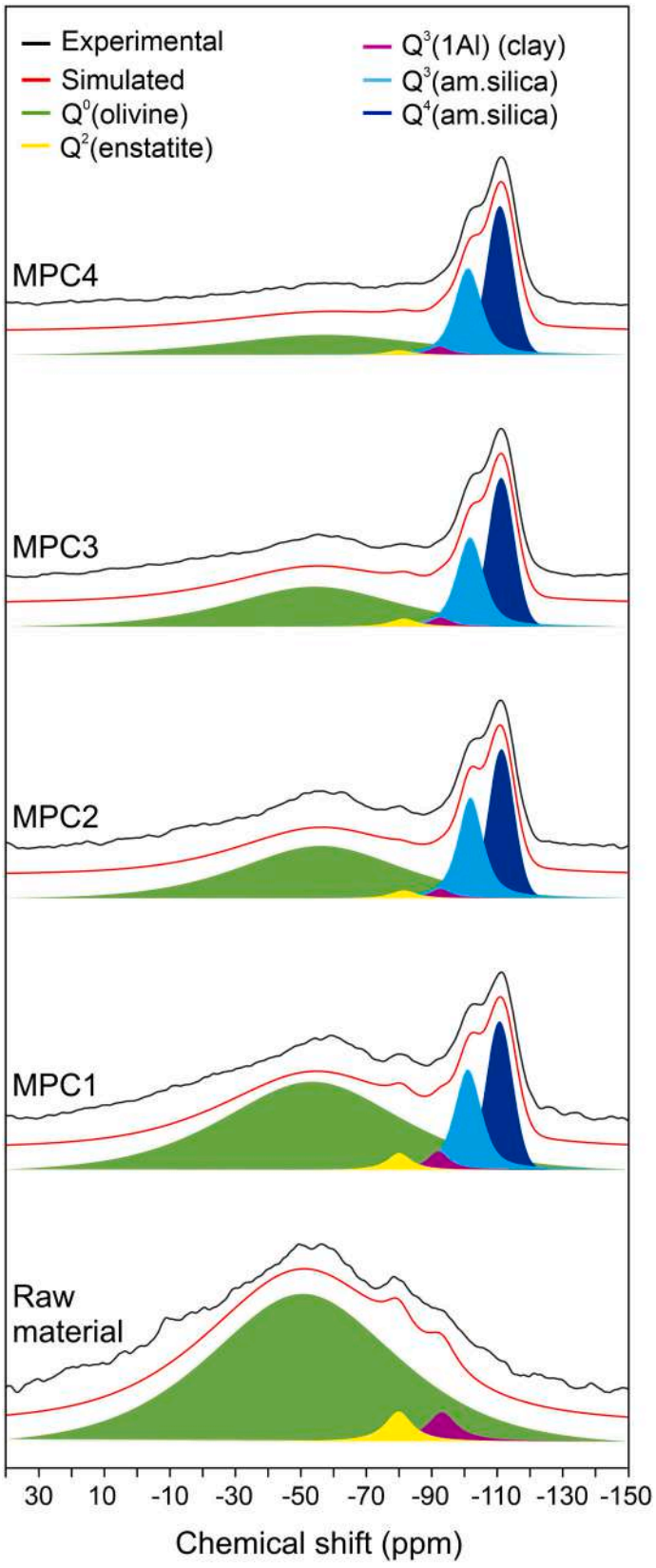

Fig. 6. ^{29}Si MAS spectra of olivine raw material and MPC samples, with deconvolution and assignments.

Table 5
Results of deconvolution of ^{29}Si MAS spectra.

	Raw material		MPC1		MPC2		MPC3		MPC4	
	δ_{iso}	Amount	δ_{iso}	Amount	δ_{iso}	Amount	δ_{iso}	Amount	δ_{iso}	Amount
	ppm	mol%	ppm	mol%	ppm	mol%	ppm	mol%	ppm	mol%
Q^0 (olivine)	−58.3	94.4	−58.3	69.1	−58.3	62.2	−58.3	60.5	−58.3	37.4
Q^2 (enstatite)	−81.9	2.4	−81.9	2.1	−81.9	2.3	−81.9	2.1	−81.9	1.5
Q^3(1Al) (clay)	−93.1	3.2	−93.1	2.1	−93.1	2.3	−93.1	2.1	−93.1	2.2
Q^3 (am. silica)	–	–	−101.3	12.3	−101.3	15.2	−101.4	15.9	−101.1	24.4
Q^4 (am. silica)	–	–	−111.7	14.4	−111.2	18.0	−111.4	19.4	−111.5	34.5

measured ought to be considered semi-quantitative [66].

Nonetheless, interesting trends, in substantial agreement with the results presented above, can be observed. The intermediate phase is present mostly in MPC1 (orange, Fig. 11), reaching 11%vol. The volume fraction of olivine (green, Fig. 11) is the highest in the sample MPC1, slightly lower in MPC2 and MPC3 and significantly lower in MPC4, as indicated by XRPD and SSNMR. The voids (blue, Fig. 11) volume fraction is confirmed to be rather low (< 5 vol%) compared with other MPCs, such as the Mg—K phosphate cements (8–14 %) [67]. Owing to the presence of cracks, the sample MPC2 exhibited the highest value.

3.5. Compressive strength

The results of compressive strength tests on the 30-days old cements are graphically illustrated in Fig. 12. By comparing the samples with the same L/S, it can be noticed that the increase in PA concentration positively impacted on the measured strength. One of the possible reasons could be the progressive decrease in the highly porous domains rich in amorphous silica described in the previous sections, thus strengthening the whole microstructure. It might be argued that these regions exerted their weakening effect mostly because of their poor internal cohesion, as well evidenced in Figs. 9 and 10. Notably, MPC2 showed worse performances than MPC3 (24 against 40 MPa), possibly due to the high number of cracks in the former, weakening the microstructure, and the highest amount of amorphous fraction in the latter, which helps compact the microstructure [7,63]. The highest value achieved by MPC4 (76 MPa) points to a strengthening effect of the concurrent increase in olivine dissolution and newberyite crystallization [13].

3.6. Thermodynamic modelling and reaction products

The results of the simulation of the forsterite reaction with PA are presented in Fig. 13 for MPC4, and as Supplementary Material Figs. S8–S10 for the other three formulations.

According to the model, at the beginning of the reaction the dissolution of forsterite immediately allows reaching the supersaturation conditions for the precipitation of silica [20,21], following the equation:

$$Mg_2SiO_4 + 4H^+ \rightarrow 2Mg^{2+}{}_{(aq)} + SiO_2 + 2H_2O \quad (1)$$

This reaction increases the pH [20,25]. When pH-values of around 3 are reached, and with an M/P molar ratio in solution of ~0.5, the precipitation of newberyite is triggered, according to the equation:

$$Mg^{2+}{}_{(aq)} + H_2PO_{4(aq)}{}^- + 3H_2O \rightarrow MgHPO_4{\cdot}3H_2O + H^+ \quad (2)$$

Reaction (2) keeps the pH at ~3.2, and up to ~50 % of forsterite is dissolved. At the same time, the Al^{3+} ions by the partial dissolution of chlorite cause precipitation of minor amounts of Al phosphate ($AlPO_4{\bullet}2H_2O$, variscite). Moreover, forsterite dissolution increases the pH and favours the replacement of newberyite with other Mg phosphate hydrates, such as $Mg_3(PO_4)_2{\bullet}8H_2O$ (bobierrite) and $Mg_3(PO_4)_2{\bullet}4H_2O$. At high forsterite conversion (> 80 %), the basic pH (8.2) induces a destabilization of the amorphous silica, which reacts with the available magnesium to precipitate poorly crystalline magnesium silicate hydrates (M-S-H) [43].

A similar pathway is predicted for MPC1, MPC2 and MPC3, but, because of the much higher overall M/P ratio (between 3.0 and 4.0) and lower L/S ratio, the stability ranges of the dissolution products are shifted towards the left side of the diagrams, owing to the more concentrated conditions (Figs. S8–S10). Altogether, this results in the anticipated precipitation of newberyite already at a forsterite reactivity degree of just 10 %, bobierrite (20–35 %) and M-S-H (30–45 %). The conditions of basic pH are reached at a lower reactivity degree of forsterite, while the $Mg_3(PO_4)_2{\bullet}4H_2O$ precipitation with respect to bobierrite is more favoured passing from MPC1 to MPC3, due to the increase in the acid concentration (i.e., lower amount of water). For the same reason, at a higher reactivity degree farringtonite is stabilized ($Mg_3(PO_4)_2$), whereas in all of the three samples the chemical conditions do not allow for a complete forsterite dissolution.

The phase assemblages of the reaction products determined by the XRPD quantitative phase analysis and those obtained by the modelling at the same degree of olivine conversion, are compared in Table 7. The model correctly predicted newberyite as the main product, although a large overestimation occurs for MPC3 (37.7 wt% against 20.1 wt%). Variscite accounts for <1 wt%, which may explain why it was not detected by XRPD, but, at the same time, this corroborates the assignment and quantification made on the ^{31}P MAS spectra (Table 4).

On the other hand, the model systematically indicates that an additional hydrate is expected to form, either bobierrite or $Mg_3(PO_4)_2{\bullet}4H_2O$, while in all the samples only newberyite was observed as a crystalline phase. This may be explained by their slow precipitation kinetics [25,42]. Alternatively, their formation can be mediated by an amorphous magnesium phosphate precursor. Transient amorphous phases have been observed during precipitation of silica, calcium carbonates, and alkaline phosphates [4,8,68]. Transition amorphous phases have already been reported in MPCs, where they are considered precursors of the crystalline reaction product K-struvite ($KH_2PO_4{\bullet}6H_2O$) [5,8,69]. They commonly form at high supersaturation levels [8,70], and frequently exhibit structural similarities with the crystalline counterpart, with which they may share the same structural units. This issue is common to all phosphate-based cements, owing to the low volume of water and fast dissolution kinetics, leading to out-of-equilibrium conditions [6,8].

Spectroscopic results suggested that an amorphous component containing P might be present, in addition to newberyite. This may explain the systematically higher content in the amorphous fraction detected by XRPD with respect to the amount predicted by the thermodynamic simulations (i.e., the precipitated silica). Although the P XANES LCF in Fig. S3 points to a bobierrite-like local environment, the chemical shift observed by ^{31}P solid-state NMR (δ_{iso} between −0.7 and − 1.5 ppm) is relatively far from the bobierrite resonance occurring at 4.5 ppm, rather suggesting the presence of an amorphous $MgHPO_4$ phase [15,47]. This is further supported by the MPC3 analysis, in which, on the one hand, the EDS investigation shows an Mg/P ratio < 1 in the amorphous regions (Fig. S5) while, on the other hand, the newberyite can describe most of the P XANES signal of the sample, even though the amorphous component is higher than the crystalline phases' (Table 4). Moreover, it is also worth considering that in MPC3 the amorphous phase may be more

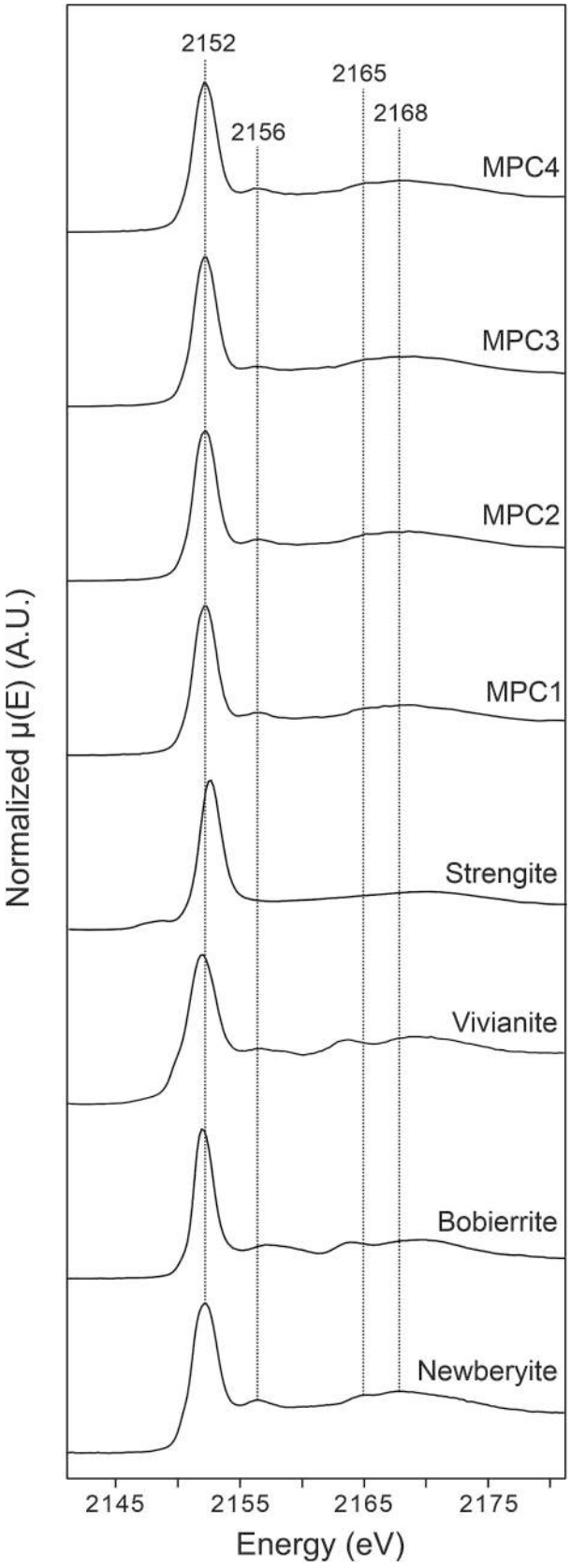

Fig. 7. P K-edge XANES spectra of the references and cement samples [31].

complex than in the other samples, given that it involves additional contributions as suggested by the different ^{31}P solid-state NMR δ_{iso} (Table 4) and TGA weight loss profile (Fig. 4).

Previous investigation on volcanic ash geopolymers have pointed out the pivotal role of Fe in strengthening the matrix, due to its readily availability in acidic environment [26,27]. Here, as olivine dissolves, it is reasonable to expect iron to be incorporated in the reaction products, since it is part of the solid solution (7 % fayalite). However, no decisive conclusion about its fate has been found with the techniques employed. In one case, NMR is severely limited in the investigation of paramagnetic species, as discussed in Section 3.3. Moreover, no pre-edge feature typical of Fe(III)-phosphate was observed in the samples P K-edge XANES spectra, while vivianite contribution may be below the detection/quantification limit of XANES LCF. In this latter case, self-absorption effects due to fluorescence detection can hamper the signal and complicate the procedure [56]. The SEM-EDS spectra and maps showed an Fe content uniformly distributed in the matrix. Although to the best of our knowledge the possible substitution of magnesium with iron in newberyite is not reported, it is proven that Fe may influence P availability/recovery in soil by precipitation of Fe(III)/Fe(II) phosphates, depending on pH and redox conditions [35,35,71]. In addition, struvite precipitation experiments in presence of Fe ions suggested competition with Mg to precipitate vivianite [72]. The EDS analysis shown in Fig. S6 points to a similar behaviour, where regions rich in Fe and P were observed. Although the Fe role in the system is of paramount importance when less pure olivine or olivine-rich waste are employed, its investigation would require more specific approaches, such Fe K-edge XAS, Electron Paramagnetic Resonance (EPR) and Mossbauer spectroscopies [73].

3.7. *Formation mechanism of olivine-phosphate cements*

Understanding the dissolution process of forsterite is crucial to develop a mechanistic model for the cement reaction. Previous works have shown that mechanisms and rates of dissolution of silicate minerals in aqueous solution depend on the connectivity of their silica framework and the characteristics of the metal-oxygen bonds [20]. As mentioned in the introduction, the structure of forsterite consists of isolated SiO_4^{4-} tetrahedra linked by Mg^{2+} cations in octahedral coordination [19]. Under acidic conditions, the less stable ionic Mg—O bonds (~3816 kJ/mol) break more easily than the covalent Si—O bonds (~13,000 kJ/mol) [21,22]. The magnesium ions are thus released from the mineral surface and form activated complexes with water. Their vacancies are replaced by protons, and the isolated SiO_4^{4-} tetrahedra enter in the solution [20]. This process is usually confined to the very surface of the grains (up to 100 nm), in contrast with the dissolution of chain-silicates, like wollastonite, which is accompanied at acidic pH by a H^+ diffusion deeper into the lattice, eventually promoting silica tetrahedral condensation [20,63]. Thus, this congruent dissolution of olivine coupled with the low solubility of silica at low pH (< 3), may produce the observed discrete silica-rich domains (Figs. 8–9), by agglomeration of submicrometric particles. This is further confirmed by ^{29}Si SSNMR, which evidenced a significant fraction of surface silanol (Q^3) groups with respect to bulk silicate (Q^4) (Table 5), as commonly found in synthetic silica nanoparticles [74,75].

The leaching of Mg^{2+} ions and the replacement with protons has been observed to come to completion in few minutes [21,22,76]. Moreover, since the concentration of the activated complexes is determined by the amount of protons and water, the dissolution rate of forsterite is influenced by pH and activity of water [20,21]. Therefore, considering the conditions of the experiments, the first exothermic event in the heat flow curves could be ascribed to this process. The successive reaction steps, in partial overlap with the first one, include the condensation of silica tetrahedra and the precipitation of amorphous and crystalline phosphates, whose presence is proven by XRPD, ^{31}P NMR and XANES. In analogy with other CBPCs, the positive enthalpy

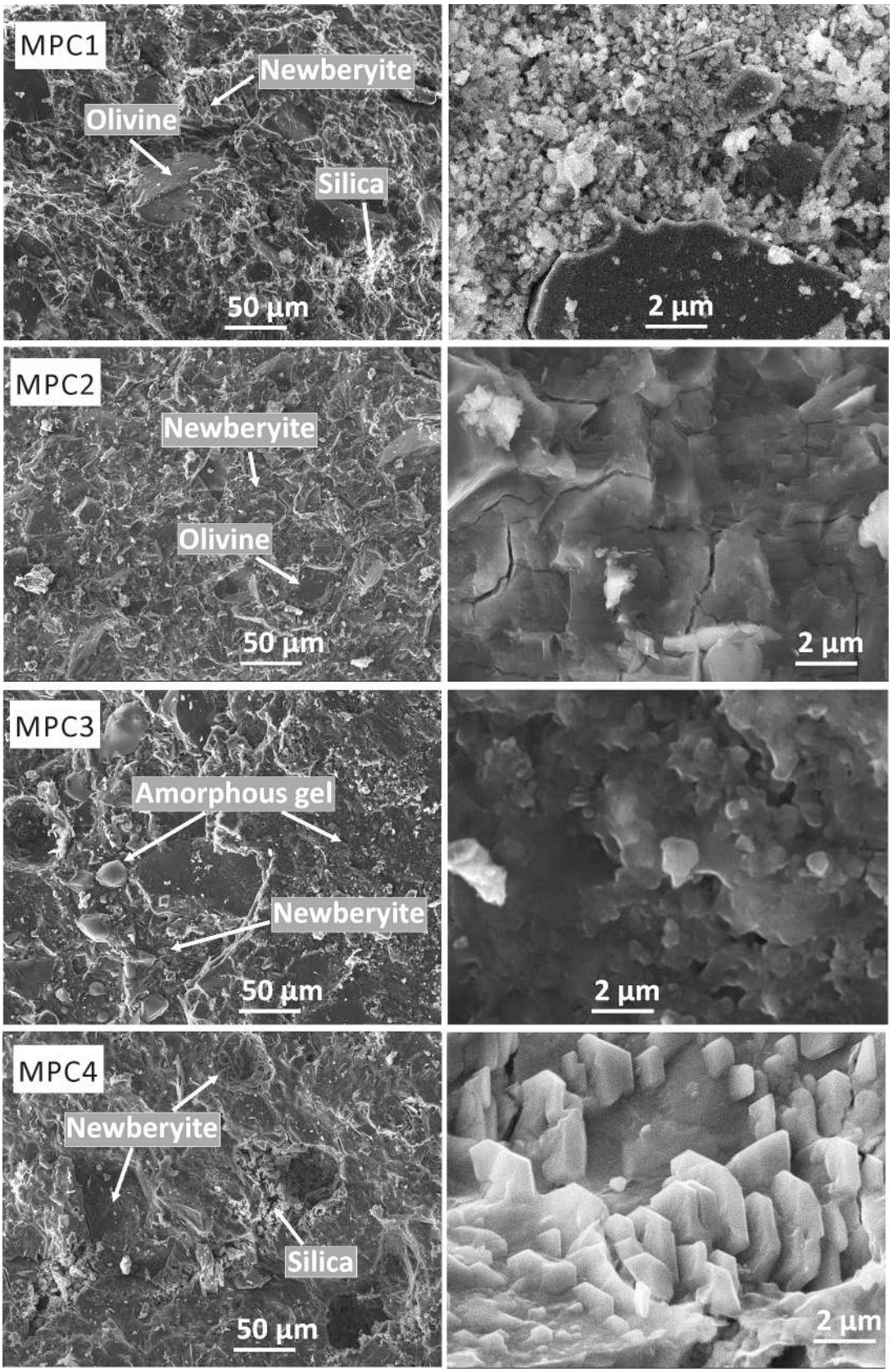

Fig. 8. SEM-SE micrographs of MPC samples, at two different magnifications.

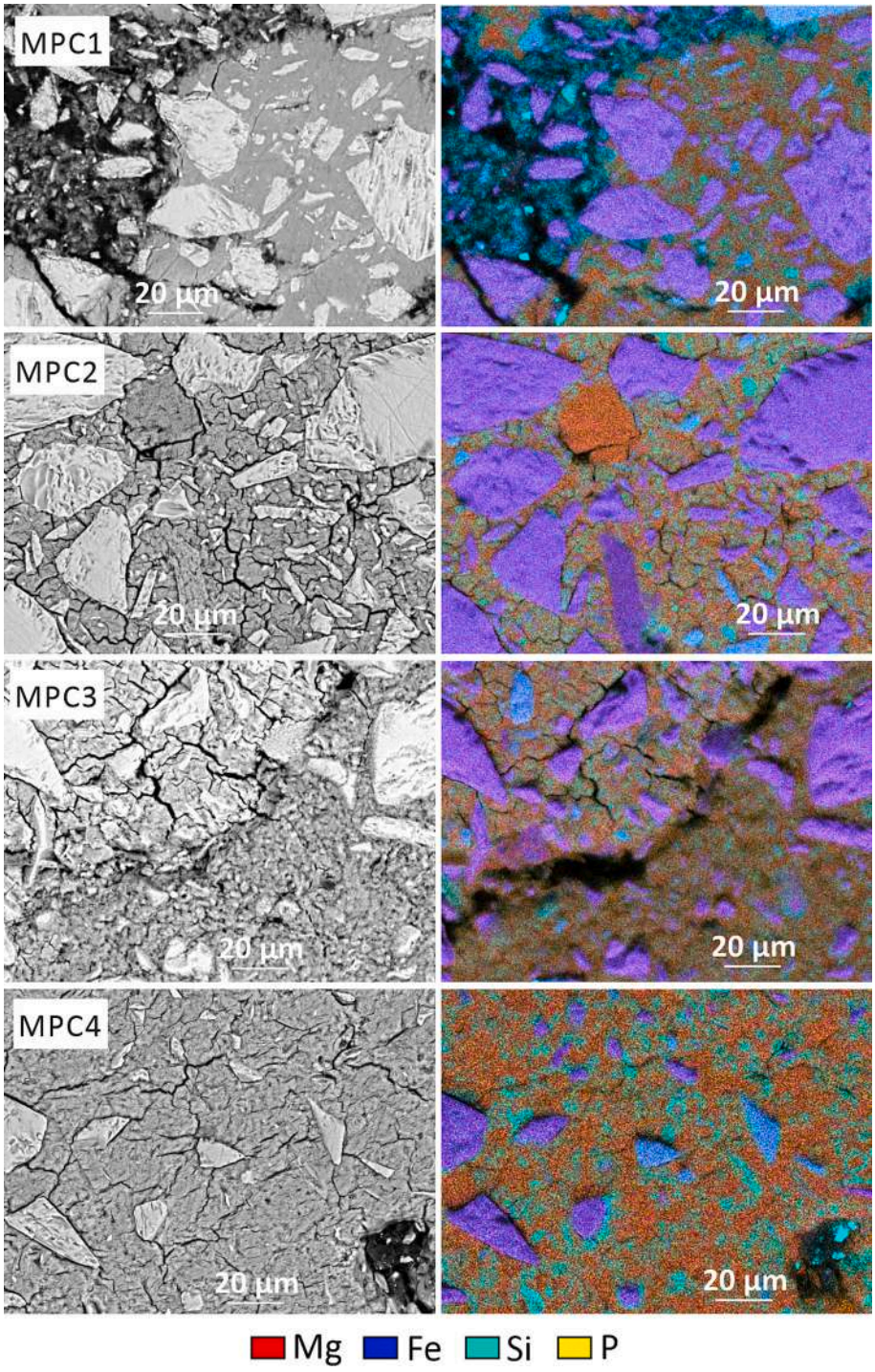

Fig. 9. SEM-BSE micrographs of MPC cross-sections together with the layered EDS maps. The selected colours allow to visualize the qualitative phase distribution, in terms of Mg—phosphate (orange),Si-rich region (light blue), olivine (violet) and enstatite (blue), (For interpretation of the references to colour in this figure legend, the reader is referred to the web version of this article.)

contribution of these reactions can be reasonably identified as the second signal observed in the calorimetric traces [5,9]. Unfortunately, no physically sound approach to disentangle the contributions of single heat flow events in the isothermal calorimetry signal have been devised yet [9]. However, for illustrative purposes, the heat flow curve of MPC2 has been fitted by two asymmetric peak functions (Fig. S11) to show that the apparently small enthalpic contribution of the process of product formation is actually of the same order of magnitude of the one due to the olivine dissolution. According to the collected experimental evidence, this second event of heat release may comprise more than one contribution, which, due to the intrinsic limitation of the method, cannot be unfolded. Overall, the rates are low but distributed over long times. This is common to other CBPC systems, in which high supersaturation levels, attained after the early dissolution steps, trigger the precipitation of the phosphates. Since this process entails the progressive conversion of water from free (in solution) to bound (into the products), the ion mobility drops, slowing down the overall kinetics [5,77,78].

The increase in acid concentration at the same L/S ratio (MPC1 to MPC3), promotes a more effective dissolution of olivine, as confirmed by

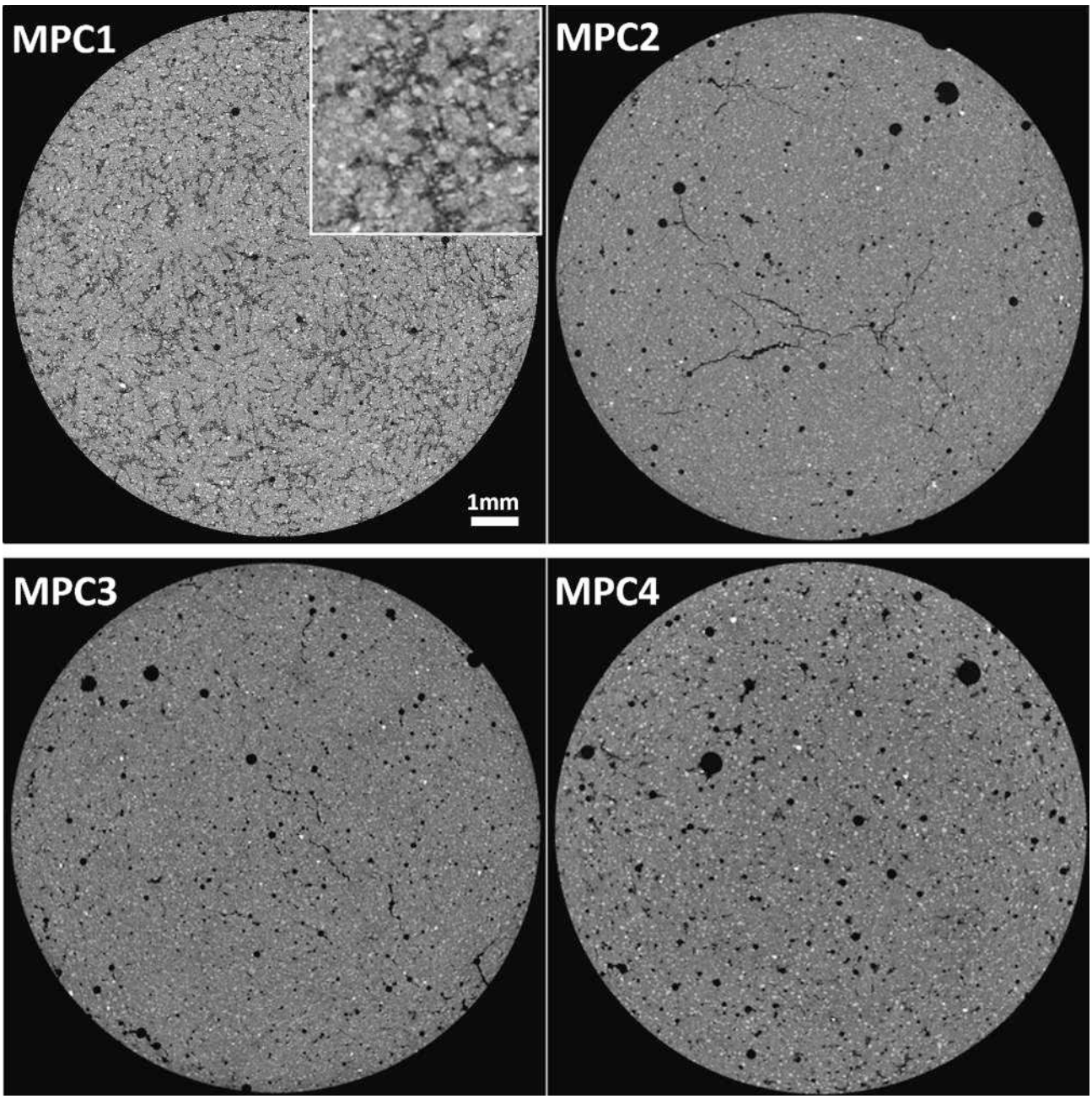

Fig. 10. CT reconstructed slices of MPCs cylinder samples.

the steeper and more "compressed" first part of the heat flow curves (Fig. 2). It follows that at equilibrium a higher amount of product is expected to form, as predicted by the thermodynamic simulations. However, as discussed in the previous section, the reaction becomes also progressively dependent on the kinetics, thus favouring amorphous over crystalline products, as well-evidenced by MPC3. The nature of the amorphous phase(s) and the conversion into crystalline phosphates, as well, are a function of the overall stoichiometry, represented by the M/P and L/S ratios. Considering the overall reaction:

$$Mg_2SiO_4 + 2H_3PO_4 + 4H_2O \rightarrow 2MgHPO_4 \bullet 3H_2O + SiO_2$$

a water/P molar ratio of 2 is necessary to precipitate newberyite. The actual molar ratio is 3.6, 2.3, 1.4 and 2.3 for MPC1, MPC2, MPC3 and MPC4, respectively (Table 2). This partly explains the differences observed in the nature of the products (including the amorphous phase, as discussed in the previous section) and in the microstructure, as revealed by SEM and CT. In fact, the relative amount of water has been found to be decisive for the optimal properties in other magnesium phosphate cements [6,78]. A large excess, as in MPC1 (3.6 against 2), increases the cement porosity due to water segregation, as it only partially binds to the hydrated products. This results in a non-uniform distribution of reaction products, thereby reducing the mechanical performance (Fig. 12). Conversely, insufficient water, as in MPC3 (1.4 against 2), inhibits the crystallization of the products, possibly by limiting the structural mobility which is often required for amorphous-crystalline transitions [5]. In this sample, the hindered crystallization reduced the amount of heat released with respect to MPC2, as evidenced by isothermal calorimetry, but was beneficial to the compressive strength (Fig. 12).

It can be conjectured that the main strengthening mechanism in the studied cements is the development of an interlocked lath-shaped microstructure resembling a composite material and encompassing an

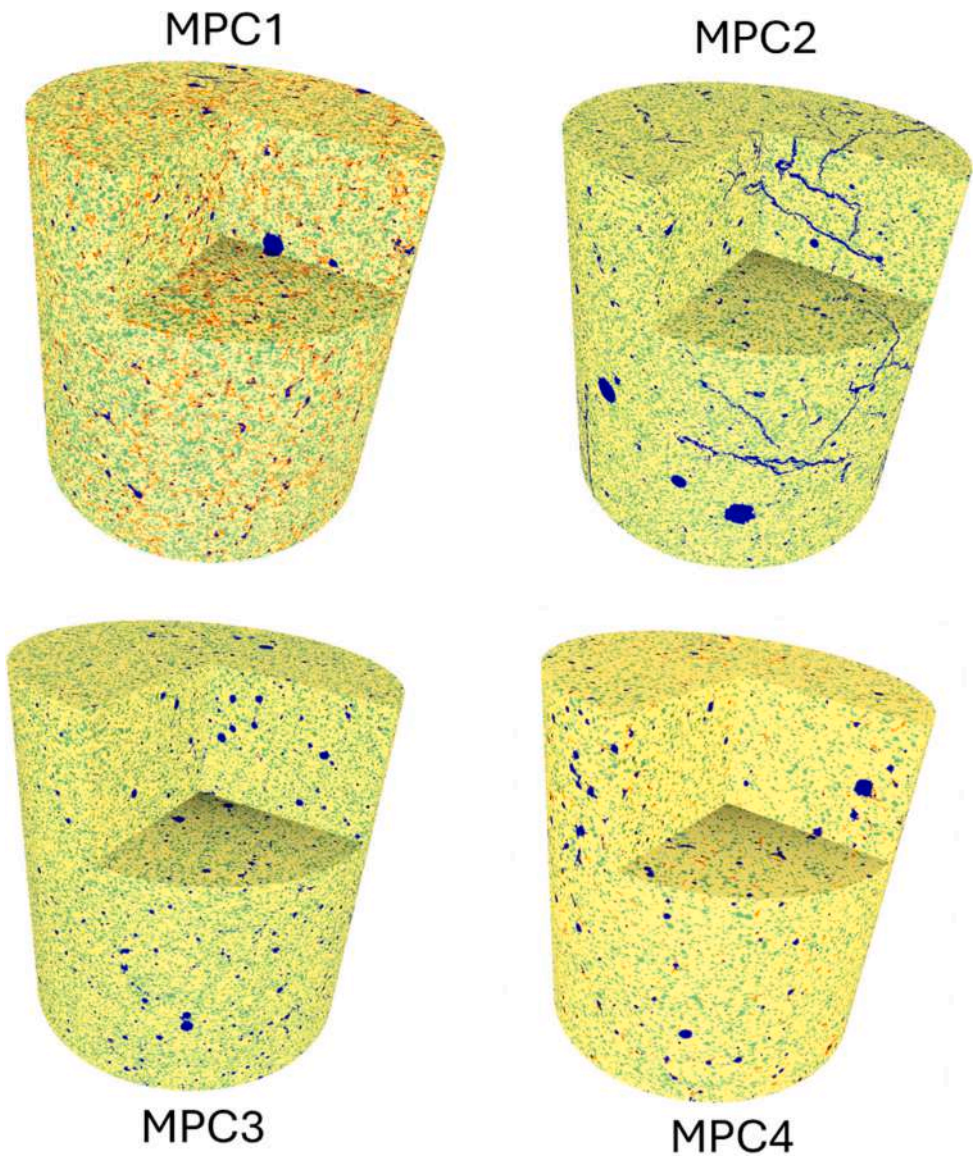

Fig. 11. 3D rendering of cylindrical ROIs with diameter 6 mm from the investigated samples. Pores: blue; intermediate region: orange; olivine crystals: green; cement matrix: yellow. (For interpretation of the references to colour in this figure legend, the reader is referred to the web version of this article.)

Table 6
Results of quantitative image analysis from CT data.

Classes	MPC1	MPC2	MPC3	MPC4
	vol%			
Matrix	60.7	72.6	73.3	82.1
Intermediate	11.2	–	0.1	2.1
Olivine	25.8	23.8	23.5	12.7
Pores	2.3	4.6	3.1	3.0

equilibrated mix of crystals embedded in the amorphous phase(s), as encountered in ceramics [79] and previously documented for other CBCs [64,67]. Although an in-depth characterization of the toughening mechanisms in the olivine-MPCs falls outside the scope of this work, it is clear that the observed strength originates from the complex interplay between several factors: i) the volume fraction of crystals and the amorphous phase; ii) the strength of the crystals, their size and habit (e.g., elongated, tabular, equant); iii) the type and amount of porosity (as discussed in Section 3.4.2). In sample MPC2, the detrimental effect of the porosity (characterized by diffuse cracks) prevails over the beneficial

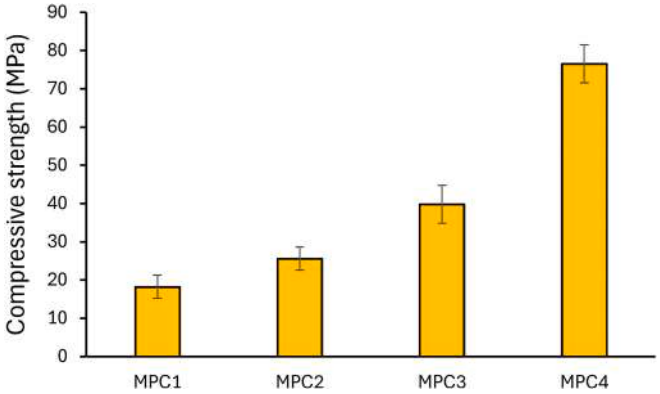

Fig. 12. Compressive strength of 30-days MPC samples.

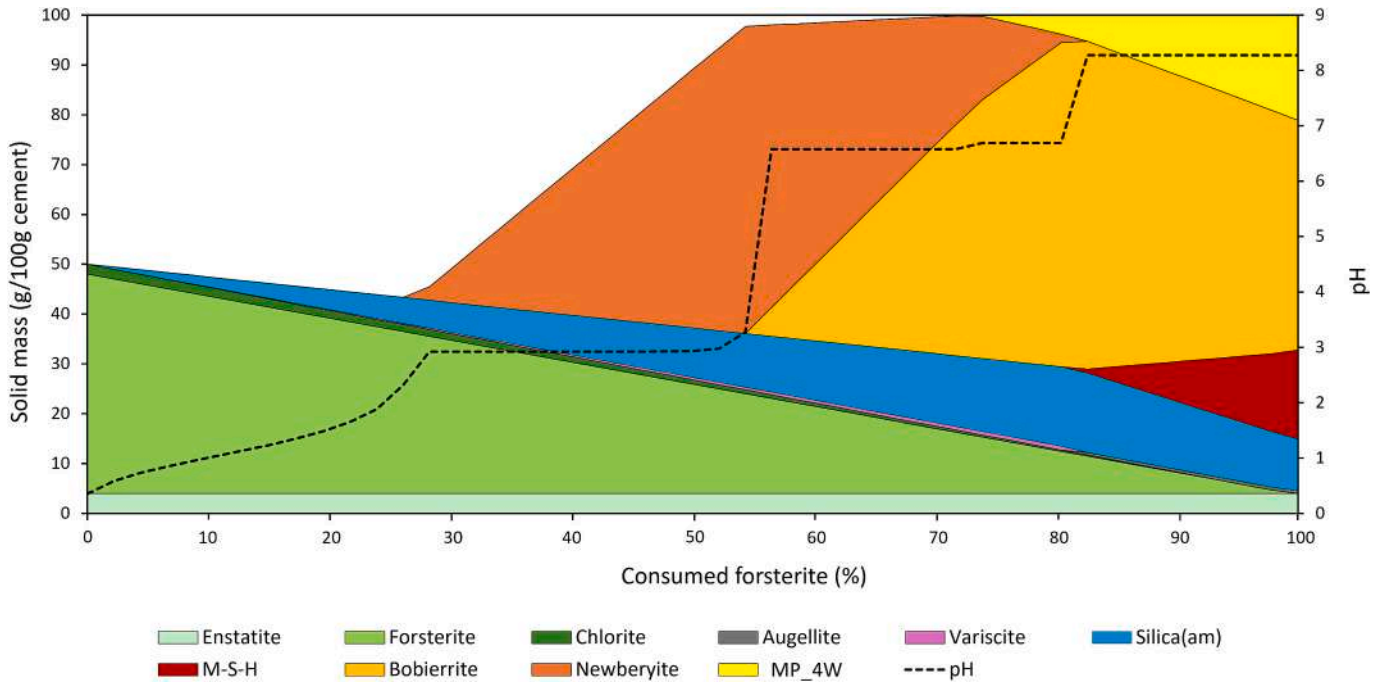

Fig. 13. Simulated pH and phase assemblage distribution as a function of forsterite reactivity for MPC4. The MP_4W in the legend represents the compound $Mg_3PO_4{\cdot}4H_2O$.

Table 7
Comparison between the experimental and simulated phase assemblages of the cement samples. The calculated residual solution is not considered.

	MPC1		MPC2		MPC3		MPC4	
	25 % consumed olivine		31 % consumed olivine		33 % consumed olivine		57 % consumed olivine	
	Measured	Simulated	Measured	Simulated	Measured	Simulated	Measured	Simulated
	wt%							
Newberyite	31.9	29.9	35.8	31.1	20.1	37.7	56.7	54.7
Variscite		0.3		0.4		0.4		0.6
Bobierrite		6.1		10.6				7.7
Farringtonite						5.2		
Silica		6.6		8		8.6		11.2
Amorphous	18.2		19.1		35		20.4	

effect of the higher amount of reaction products and the nearly stoichiometric water/P molar ratio (which reduced water segregation). Conversely, the optimal performance of MPC4 can be ascribed to the formulation with an almost stoichiometric amount of water, a high olivine consumption, newberyite precipitation and the near absence of cracks. When compared with the MPCs based on (K-)struvite, this implies a more substantial consumption of phosphates, as they usually employ MgO:phosphate mass ratio around 3 [80]. Although this may appear unfavorable, similar values have been obtained when olivine-rich waste, like volcanic ash, was reacted with phosphoric acid (mass ratio 3:1, 2:1), highlighting the potential of this reaction [26–29].

4. Conclusions

In this work, the cementitious properties of Mg-olivine when mixed with phosphoric acid are investigated. The following conclusions have been derived:

- Curing at 60 °C leads to relatively fast-setting cements, a process triggered by the increase in the olivine dissolution rate induced by the very low pH and favoured by the curing temperature.
- The Mg^{2+} ions released in solution favours the precipitation of newberyite ($MgHPO_4 \bullet 3H_2O$), whereas the isolated SiO_4^{4-} tetrahedra of olivine are first released into solution and then precipitated as amorphous silica particles. The former is mostly crystalline, but solid-state NMR measurements suggested the presence also of a fraction of amorphous $MgHPO_4$, which becomes preponderant when a very high acid concentration (80 wt%) is employed.
- The cement microstructure is composed by sub-micrometric silica particles dispersed in a matrix of densely packed micrometric tabular newberyite crystals, together with unreacted olivine crystals. The dissolved iron is suggested to become bound to the phosphate, although no decisive conclusion could be obtained with the analytical techniques employed.
- The thermodynamic modelling well predicted the observed phase assemblages, although with some discrepancies due to kinetic aspects, which grows in importance increasing the acid concentration.
- At constant L/S ratio, a water/P molar ratio significantly larger than 2, which is stoichiometric with respect to newberyite, induces water segregation and increases porosity, thus impacting negatively on compressive strength. Conversely, for water/$P < 1.4$ the newberyite crystallization is hindered, increasing amorphous content and mechanical strength. A maximum of 75 MPa was obtained with an M/P molar ratio of 1.7 and water/P molar ratio of 2.3.

Although further studies regarding durability and optimization of

the formulation are needed, the results here presented suggest that olivine may be a viable alternative to the magnesium oxide in the reaction to produce MPCs. Moreover, they may provide useful information for better understanding olivine-rich waste reactivity under acidic conditions in view of their recycling in phosphate binders.

Funding

The present study (AP) has been partly funded by Ministero della Transizione Ecologica through the call: "CLEAN – Ceneri Leggere Eco-sostenibili per un Ambiente No-rifiuti" (m_amte.MiTE.REGISTRO UFFICIALE.USCITA.0049573.22-04-2022).

CRediT authorship contribution statement

Davide Bernasconi: Writing – review & editing, Writing – original draft, Visualization, Validation, Methodology, Investigation, Formal analysis, Data curation, Conceptualization. **Alberto Viani:** Writing – review & editing, Writing – original draft, Supervision, Resources, Methodology, Formal analysis, Conceptualization. **Lucie Zárybnická:** Writing – review & editing, Investigation. **Simone Bordignon:** Writing – review & editing, Investigation. **Jose R.A. Godinho:** Writing – review & editing, Investigation. **Alexey Maximenko:** Investigation. **Cem Celikutku:** Investigation. **Sadaf Fatima Jafri:** Investigation. **Elisa Borfecchia:** Writing – review & editing, Investigation. **Quentin Wehrung:** Investigation. **Roberto Gobetto:** Writing – review & editing, Resources. **Alessandro Pavese:** Writing – review & editing, Supervision, Resources, Project administration, Funding acquisition.

Declaration of competing interest

The authors declare that they have no known competing financial interests or personal relationships that could have appeared to influence the work reported in this paper.

Data availability

Data will be made available on request.

Acknowledgements

We acknowledge CERIC platform and SOLARIS National Synchrotron Radiation Centre for providing access to the beamline (proposal nr. 20232162) and for financial support. The XANES measurements at ASTRA beamline were made under the provision of the Polish Ministry of Education and Science project: 'Support for research and development with the use of research infrastructure of the National Synchrotron Radiation Centre SOLARIS' under contract nr 1/SOL/2021/2. The further development of the ASTRA beamline for measuring at low photon energies was supported within the EU Horizon2020 programme (952148-Sylinda). CT results were granted via the EXCITE network, which received funding from the European Union's Horizon 2020 research and innovation programme under grant agreement no. 101005611. L.Z. gratefully acknowledges support from the Czech Academy of Sciences, Institute of Theoretical and Applied Mechanics-RVO 68378297. D.B. thanks Dr. Nadia Curetti for useful discussion. D.B. and A.V. thanks Sibelco, in the person of Davide Venturelli and Francesco Ferrari for providing the natural olivine used in this study.

Appendix A. Supplementary data

Supplementary data to this article can be found online at https://doi.org/10.1016/j.cemconres.2024.107694.

References

[1] C. Shi, B. Qu, J.L. Provis, Recent progress in low-carbon binders, Cem. Concr. Res. 122 (2019) 227–250, https://doi.org/10.1016/j.cemconres.2019.05.009.
[2] S.A. Miller, R.J. Myers, Environmental impacts of alternative cement binders, Environ. Sci. Technol. 54 (2019) 677–686, https://doi.org/10.1021/acs.est.9b05550.
[3] A.S. Wagh, Recent progress in chemically bonded phosphate ceramics, ISRN Ceramics 2013 (2013) 1–20, https://doi.org/10.1155/2013/983731.
[4] A.S. Wagh, S.Y. Jeong, Chemically Bonded Phosphate Ceramics: i, A Dissolution Model of Formation, J. Am. Ceram. Soc. 86 (2003) 1838–1844, https://doi.org/10.1111/j.1151-2916.2003.tb03569.x.
[5] A. Viani, P. Mácová, Polyamorphism and frustrated crystallization in the acid–base reaction of magnesium potassium phosphate cements, CrystEngComm 20 (2018) 4600–4613, https://doi.org/10.1039/c8ce00670a.
[6] B. Xu, F. Winnefeld, J. Kaufmann, B. Lothenbach, Influence of magnesium-to-phosphate ratio and water-to-cement ratio on hydration and properties of magnesium potassium phosphate cements, Cem. Concr. Res. 123 (2019) 105781, https://doi.org/10.1016/j.cemconres.2019.105781.
[7] A.S. Wagh, Chemically Bonded Phosphate Ceramics: Twenty-First Century Materials with Diverse Applications. http://ci.nii.ac.jp/ncid/BA73891754, 2004.
[8] A.D. Wilson, J.W. Nicholson, Acid-Base cements, 1993, https://doi.org/10.1017/cbo9780511524813.
[9] P. Laniesse, C.C.D. Coumes, A. Poulesquen, A. Bourchy, A. Mesbah, G.L. Saout, P. Gaveau, Setting and hardening process of a wollastonite-based brushite cement, Cem. Concr. Res. 106 (2018) 65–76, https://doi.org/10.1016/j.cemconres.2018.01.019.
[10] Y.-S. Wang, Y. Alrefaei, J.-G. Dai, Silico-Aluminophosphate and Alkali-Aluminosilicate geopolymers: A Comparative review, Frontiers in Materials 6, 2019, https://doi.org/10.3389/fmats.2019.00106.
[11] H. Lin, H. Liu, Y. Li, X. Kong, Properties and reaction mechanism of phosphoric acid activated metakaolin geopolymer at varied curing temperatures, Cem. Concr. Res. 144 (2021) 106425, https://doi.org/10.1016/j.cemconres.2021.106425.
[12] D. Bernasconi, A. Viani, L. Zárybnická, P. Mácová, S. Bordignon, C. Caviglia, E. Destefanis, R. Gobetto, A. Pavese, Phosphate-based geopolymer: Influence of municipal solid waste fly ash introduction on structure and compressive strength, Ceram. Int. 49 (2023) 22149–22159, https://doi.org/10.1016/j.ceramint.2023.04.042.
[13] S.A. Walling, J.L. Provis, Magnesia-Based Cements: a journey of 150 years, and cements for the future? Chem. Rev. 116 (2016) 4170–4204, https://doi.org/10.1021/acs.chemrev.5b00463.
[14] E. Bernard, H. Nguyen, S. Kawashima, B. Lothenbach, H. Manzano, J. Provis, A. Scott, C. Unluer, F. Winnefeld, P. Kinnunen, MgO-based cements – Current status and opportunities, RILEM Techn. Lett. 8 (2023) 65–78, https://doi.org/10.21809/rilemtechlett.2023.177.
[15] H. Lahalle, C.C.D. Coumes, C. Mercier, D. Lambertin, C. Cannes, S. Delpech, S. Gauffinet, Influence of the w/c ratio on the hydration process of a magnesium phosphate cement and on its retardation by boric acid, Cem. Concr. Res. 109 (2018) 159–174, https://doi.org/10.1016/j.cemconres.2018.04.010.
[16] B. Xu, B. Lothenbach, H. Ma, Properties of fly ash blended magnesium potassium phosphate mortars: Effect of the ratio between fly ash and magnesia, Cem. Concr. Compos. 90 (2018) 169–177, https://doi.org/10.1016/j.cemconcomp.2018.04.002.
[17] B. Xu, F. Winnefeld, B. Ma, D. Rentsch, B. Lothenbach, Influence of aluminum sulfate on properties and hydration of magnesium potassium phosphate cements, Cem. Concr. Res. 156 (2022) 106788, https://doi.org/10.1016/j.cemconres.2022.106788.
[18] F. Qiao, C.K. Chau, Z. Li, Property evaluation of magnesium phosphate cement mortar as patch repair material, Constr. Build. Mater. 24 (2010) 695–700, https://doi.org/10.1016/j.conbuildmat.2009.10.039.
[19] Encyclopedia of Geology, Academic Press, 2020.
[20] E.H. Oelkers, J. Declercq, G.D. Saldi, S.R. Gislason, J. Schott, Olivine dissolution rates: A critical review, Chem. Geol. 500 (2018) 1–19, https://doi.org/10.1016/j.chemgeo.2018.10.008.
[21] Q.R.S. Miller, H.T. Schaef, J.P. Kaszuba, G. Gadikota, B.P. McGrail, K.M. Rosso, Quantitative review of olivine carbonation Kinetics: reactivity trends, mechanistic insights, and research frontiers, Environ. Sci. Technol. Lett. 6 (2019) 431–442, https://doi.org/10.1021/acs.estlett.9b00301.
[22] F. Wang, D. Dreisinger, M. Jarvis, T. Hitchins, Kinetics and mechanism of mineral carbonation of olivine for CO_2 sequestration, Miner. Eng. 131 (2019) 185–197, https://doi.org/10.1016/j.mineng.2018.11.024.
[23] Y.X. Chen, S. Li, B. Mezari, E.J.M. Hensen, R. Yu, K. Schollbach, H.J.H. Brouwers, Q. Yu, Effect of highly dispersed colloidal olivine nano-silica on early age properties of ultra-high performance concrete, Cem. Concr. Compos. 131 (2022) 104564, https://doi.org/10.1016/j.cemconcomp.2022.104564.
[24] S.A. Nye, S. Vineet, O. Christopher, S. Barnaby, C. Chris, Use of Olivine for the production of MgO-SiO_2 binders, Frontiers in Built Environment 7, 2021, https://doi.org/10.3389/fbuil.2021.640243.
[25] P. Laniesse, C.C.D. Coumes, G.L. Saout, A. Mesbah, Understanding the setting and hardening process of wollastonite-based brushite cement. Part 1: Influence of the Ca/P ratio and H_3PO_4 concentration of the mixing solution, Cement and Concrete Research 134 (2020) 106094. https://doi.org/10.1016/j.cemconres.2020.106094.
[26] J.N.Y. Djobo, D. Stephan, Understanding the binder chemistry, microstructure, and physical properties of volcanic ash phosphate geopolymer binder, J. Am. Ceram. Soc. 105 (2022) 3226–3237, https://doi.org/10.1111/jace.18333.

[27] J.N.Y. Djobo, D. Stephan, A. Elimbi, Setting and hardening behavior of volcanic ash phosphate cement, J. Build. Eng. 31 (2020) 101427, https://doi.org/10.1016/j.jobe.2020.101427.
[28] J.N.Y. Djobo, D. Stephan, Control of the setting reaction and strength development of slag-blended volcanic ash-based phosphate geopolymer with the addition of boric acid, J. Aust. Ceram. Soc. 57 (2021) 1145–1154, https://doi.org/10.1007/s41779-021-00610-4.
[29] J.N.Y. Djobo, D. Stephan, The reaction of calcium during the formation of metakaolin phosphate geopolymer binder, Cem. Concr. Res. 158 (2022) 106840, https://doi.org/10.1016/j.cemconres.2022.106840.
[30] E. Furlani, M. Magnan, E. Mingone, M. Deison, E. Aneggi, F. Andreatta, L. Fedrizzi, S. Maschio, Waste olivine and silica sands boost geopolymers' performances: experimental investigation, Int. J. Environ. Stud. 76 (2019) 491–506, https://doi.org/10.1080/00207233.2019.1585156.
[31] B. Walkley, J.L. Provis, Solid-state nuclear magnetic resonance spectroscopy of cements, Mater. Today Adv. 1 (2019) 100007, https://doi.org/10.1016/j.mtadv.2019.100007.
[32] D. Massiot, F. Fayon, M. Capron, I. King, S.L. Calvé, B. Alonso, J.-O. Durand, B. Bujoli, Z. Gan, G. Hoatson, Modelling one- and two-dimensional solid-state NMR spectra, Magn. Reson. Chem. 40 (2001) 70–76, https://doi.org/10.1002/mrc.984.
[33] B. Ravel, M. Newville, ATHENA, ARTEMIS, HEPHAESTUS: data analysis for X-ray absorption spectroscopy using IFEFFIT, J. Synchrotron Radiat. 12 (2005) 537–541, https://doi.org/10.1107/s0909049505012719.
[34] C. Vogel, C. Rivard, V. Wilken, A. Muskolus, C. Adam, Performance of secondary P-fertilizers in pot experiments analyzed by phosphorus X-ray absorption near-edge structure (XANES) spectroscopy, Ambio 47 (2017) 62–72, https://doi.org/10.1007/s13280-017-0973-z.
[35] M. Egger, T. Jilbert, T. Behrends, C. Rivard, C.P. Slomp, Vivianite is a major sink for phosphorus in methanogenic coastal surface sediments, Geochim. Cosmochim. Acta 169 (2015) 217–235, https://doi.org/10.1016/j.gca.2015.09.012.
[36] C. Rivard, B. Lanson, M. Cotte, Phosphorus speciation and micro-scale spatial distribution in North-American temperate agricultural soils from micro X-ray fluorescence and X-ray absorption near-edge spectroscopy, Plant Soil 401 (2015) 7–22, https://doi.org/10.1007/s11104-015-2494-5.
[37] J. Schindelin, I. Arganda-Carreras, E. Frise, V. Kaynig, M. Longair, T. Pietzsch, S. Preibisch, C. Rueden, S. Saalfeld, B. Schmid, J.-Y. Tinevez, D.J. White, V. Hartenstein, K. Eliceiri, P. Tomancak, A. Cardona, Fiji: an open-source platform for biological-image analysis, Nat. Methods 9 (2012) 676–682, https://doi.org/10.1038/nmeth.2019.
[38] Dragonfly 2024.1 [Windows]. Comet Technologies Canada Inc., Montreal, Canada; software available at. https://dragonfly.comet.tech/J.
[39] D.A. Kulik, T. Wagner, S.V. Dmytrieva, G. Kosakowski, F.F. Hingerl, K. V. Chudnenko, U.R. Berner, GEM-Selektor geochemical modeling package: revised algorithm and GEMS3K numerical kernel for coupled simulation codes, Comput. Geosci. (2012), https://doi.org/10.1007/s10596-012-9310-6.
[40] T. Thoenen, W. Hummel, U. Berner, E. Curti, The PSI/Nagra chemical thermodynamic database 12/07, Paul Scherrer Institut, Villigen PSI, Switzerland, 2014. Report No.: 14-04.
[41] B. Lothenbach, D.A. Kulik, T. Matschei, M. Balonis, L. Baquerizo, B. Dilnesa, G. D. Miron, R.J. Myers, Cemdata18: A chemical thermodynamic database for hydrated Portland cements and alkali-activated materials, Cem. Concr. Res. 115 (2019) 472–506, https://doi.org/10.1016/j.cemconres.2018.04.018.
[42] B. Lothenbach, B. Xu, F. Winnefeld, Thermodynamic data for magnesium (potassium) phosphates, Appl. Geochem. 111 (2019) 104450, https://doi.org/10.1016/j.apgeochem.2019.104450.
[43] E. Bernard, B. Lothenbach, C. Cau-Dit-Coumes, C. Chlique, A. Dauzeres, I. Pochard, Magnesium and calcium silicate hydrates, Part I: Investigation of the possible magnesium incorporation in calcium silicate hydrate (C-S-H) and of the calcium in magnesium silicate hydrate (M-S-H), Appl. Geochem. 89 (2018) 229–242, https://doi.org/10.1016/j.apgeochem.2017.12.005.
[44] D. Kremer, S. Etzold, J. Boldt, P. Blaum, K.M. Hahn, H. Wotruba, R. Telle, Geological mapping and characterization of possible primary input materials for the mineral sequestration of carbon dioxide in Europe, Minerals 9 (2019) 485, https://doi.org/10.3390/min9080485.
[45] R.L. Frost, S.J. Palmer, R.E. Pogson, Thermal Stability of newberyite $Mg(PO_3OH)\cdot 3H_2O$, J. Therm. Anal. Calorim. 107 (2011) 1143–1146, https://doi.org/10.1007/s10973-011-1593-7.
[46] A. German, F. Winnefeld, P. Lura, D. Rentsch, B. Lothenbach, Hydrous carbonate-containing brucite (HCB) in MgO/hydromagnesite blends, Cem. Concr. Res. 173 (2023) 107304, https://doi.org/10.1016/j.cemconres.2023.107304.
[47] S.N. Scrimgeour, J.A. Chudek, C.H. Lloyd, The determination of phosphorus containing compounds in dental casting investment products by ^{31}P solid-state MAS-NMR spectroscopy, Dent. Mater. 23 (2007) 415–424, https://doi.org/10.1016/j.dental.2006.02.010.
[48] K. Chen, A Practical review of NMR lineshapes for spin-1/2 and quadrupolar nuclei in disordered materials, Int. J. Mol. Sci. 21 (2020) 5666, 10.3390/ijms21165666.
[49] J.F. Stebbins, W.R. Panero, J.R. Smyth, D.J. Frost, Forsterite, wadsleyite, and ringwoodite (Mg_2SiO_4): ^{29}Si NMR constraints on structural disorder and effects of paramagnetic impurity ions, Am. Mineral. 94 (2009) 626–629, https://doi.org/10.2138/am.2009.3140.
[50] K. Begaudeau, Y. Morizet, P. Florian, M. Paris, J.-C. Mercier, Solid-state NMR analysis of Fe-bearing minerals: implications and applications for Earth sciences, Eur. J. Mineral. 24 (2012) 535–550, https://doi.org/10.1127/0935-1221/2012/0024-2192.
[51] W.P. Aue, A.H. Roufosse, M.J. Glimcher, R.G. Griffin, Solid-state phosphorus-31 nuclear magnetic resonance studies of synthetic solid phases of calcium phosphate: potential models of bone mineral, Biochemistry 23 (1984) 6110–6114, https://doi.org/10.1021/bi00320a032.
[52] Y. Yu, H. Guo, M. Pujari-Palmer, B. Stevensson, J. Grins, H. Engqvist, M. Edén, Advanced solid-state $^{1}H/^{31}P$ NMR characterization of pyrophosphate-doped calcium phosphate cements for biomedical applications: The structural role of pyrophosphate, Ceram. Int. 45 (2019) 20642–20655, https://doi.org/10.1016/j.ceramint.2019.07.047.
[53] G. Rim, A.K. Marchese, P. Stallworth, S.G. Greenbaum, A.-H.A. Park, ^{29}Si solid state MAS NMR study on leaching behaviors and chemical stability of different Mg-silicate structures for CO_2 sequestration, Chem. Eng. J. 396 (2020) 125204, https://doi.org/10.1016/j.cej.2020.125204.
[54] J. Li, K. Xu, G. Geng, H.E. Mason, Determine the coordination of Al and Si of Fe-rich fly ash: The challenge in NMR and how we probe its heterogeneity using X-ray spectromicroscopy, Cem. Concr. Res. 161 (2022) 106947, https://doi.org/10.1016/j.cemconres.2022.106947.
[55] D.M. Hilger, J.G. Hamilton, D. Peak, The Influences of Magnesium upon Calcium Phosphate Mineral Formation and Structure as Monitored by X-ray and Vibrational Spectroscopy, Soil Syst. 4 (2020) 8, https://doi.org/10.3390/soilsystems4010008.
[56] J.P. Gustafsson, S. Braun, J.R.M. Tuyishime, G.A. Adediran, R. Warrinnier, D. Hesterberg, A Probabilistic Approach to Phosphorus Speciation of Soils Using P K-edge XANES Spectroscopy with Linear Combination Fitting, Soil Syst. 4 (2020) 26, https://doi.org/10.3390/soilsystems4020026.
[57] K.A. Lomachenko, E. Borfecchia, C. Negri, G. Berlier, C. Lamberti, P. Beato, H. Falsig, S. Bordiga, The CU-CHA DeNOx catalyst in action: Temperature-Dependent NH_3-Assisted Selective catalytic reduction monitored by Operando XAS and XES, J. Am. Chem. Soc. 138 (2016) 12025–12028, https://doi.org/10.1021/jacs.6b06809.
[58] I. Minkoff, B. Lux, Instability criteria for growth of a hopper crystal related to spiral eutectic morphology, J. Cryst. Growth 22 (1974) 163–165, https://doi.org/10.1016/0022-0248(74)90134-1.
[59] L. Mo, L. Lv, M. Deng, J. Qian, Influence of fly ash and metakaolin on the microstructure and compressive strength of magnesium potassium phosphate cement paste, Cem. Concr. Res. 111 (2018) 116–129, https://doi.org/10.1016/j.cemconres.2018.06.003.
[60] B. Xu, H. Ma, H. Shao, Z. Li, B. Lothenbach, Influence of fly ash on compressive strength and micro-characteristics of magnesium potassium phosphate cement mortars, Cem. Concr. Res. 99 (2017) 86–94, https://doi.org/10.1016/j.cemconres.2017.05.008.
[61] D. Bernasconi, A. Viani, L. Zárybnická, P. Mácová, S. Bordignon, G. Das, E. Borfecchia, M. Štefančič, C. Caviglia, E. Destefanis, A. Bernasconi, R. Gobetto, A. Pavese, Reactivity of MSWI-fly ash in Mg-K-phosphate cement, Constr. Build. Mater. 409 (2023) 134082, https://doi.org/10.1016/j.conbuildmat.2023.134082.
[62] H. Lin, H. Liu, Y. Li, X. Kong, Properties and reaction mechanism of phosphoric acid activated metakaolin geopolymer at varied curing temperatures, Cem. Concr. Res. 144 (2021) 106425, https://doi.org/10.1016/j.cemconres.2021.106425.
[63] P. Laniesse, C.C.D. Coumes, G.L. Saout, A. Mesbah, Understanding the setting and hardening process of wollastonite-based brushite cement. Part 2: Influence of the boron and aluminum concentrations in the mixing solution, Cem. Concr. Res. 140 (2021) 106288, https://doi.org/10.1016/j.cemconres.2020.106288.
[64] J.E. Trageser, C.A. Mitchell, R.E. Jones, E.N. Matteo, J.M. Rimsza, L.J. Pyrak-Nolte, The effect of differential mineral shrinkage on crack formation and network geometry, Scientific Reports 12, 2022, 10.1038/s41598-022-23789-3.
[65] R.W. Rice, Pores as fracture origins in ceramics, J. Mater. Sci. 19 (1984) 895–914, https://doi.org/10.1007/bf00540460.
[66] J.R.A. Godinho, A. Hassanzadeh, T. Heinig, 3D quantitative mineral characterization of particles using X-Ray computed tomography, Nat. Resour. Res. 32 (2023) 479–499, https://doi.org/10.1007/s11053-023-10169-5.
[67] A. Viani, G. Lanzafame, D. Chateigner, Y.E. Mendili, K. Sotiriadis, L. Mancini, M. Zucali, B. Ouladdiaf, Microstructural evolution and texture analysis of magnesium phosphate cement, J. Am. Ceram. Soc. 103 (2019) 1414–1424, https://doi.org/10.1111/jace.16782.
[68] A. Navrotsky, Energetic clues to pathways to biomineralization: Precursors, clusters, and nanoparticles, Proc. Natl. Acad. Sci. USA 101 (2004) 12096–12101, https://doi.org/10.1073/pnas.0404778101.
[69] A. Viani, G. Mali, P. Mácová, Investigation of amorphous and crystalline phosphates in magnesium phosphate ceramics with solid-state 1H and 31P NMR spectroscopy, Ceram. Int. 43 (2017) 6571–6579, https://doi.org/10.1016/j.ceramint.2017.02.087.
[70] D. Levy, M, Zayat, The Sol-Gel Handbook, Synthesis, Characterization and Applications, 2015.
[71] L. Korving, M. Van Loosdrecht, P. Wilfert, Effect of Iron on Phosphate Recovery from Sewage Sludge, in: Springer eBooks, 2018, pp. 303–326, https://doi.org/10.1007/978-981-10-8031-9_21.
[72] D.S. Perwitasari, S. Muryanto, W.W. Schmahl, J. Jamari, A.P. Bayuseno, A kinetic and structural analysis of the effects of Ca- and Fe ions on struvite crystal growth, Solid State Sci. 134 (2022) 107062, 10.1016/j.solidstatesciences.2022.107062.
[73] A. Baral, C. Pesce, A.S. Yorkshire, Z. Zhakiyeva, R. Snellings, T. Hanein, J.L. Provis, A. Peys, Characterisation of iron-rich cementitious materials, Cem. Concr. Res. 177 (2024) 107419, https://doi.org/10.1016/j.cemconres.2023.107419.
[74] A. Coloma, A. Velty, U. Díaz, Hybrid organic–inorganic nanoparticles with associated functionality for catalytic transformation of biomass substrates, RSC Adv. 13 (2023) 10144–10156, https://doi.org/10.1039/d3ra01486j.
[75] E.G. Vieira, I.V. Soares, N.C. Da Silva, S.D. Perujo, D.R.D. Carmo, N.L.D. Filho, Synthesis and characterization of 3-[(thiourea)-propyl]-functionalized silica gel and its application in adsorption and catalysis, New J. Chem. 37 (2013) 1933, https://doi.org/10.1039/c3nj00083d.

[76] A. Blum, A. Lasaga, Role of surface speciation in the low-temperature dissolution of minerals, Nature 331 (1988) 431–433, https://doi.org/10.1038/331431a0.
[77] J.W. Nicholson, Maturation processes in glass-ionomer dental cements, Acta Biomater. Odontol. Scand. 4 (2018) 63–71, https://doi.org/10.1080/23337931.2018.1497492.
[78] X. Meng, Y. Jiang, B. Chen, L. Wang, Research progress on the setting time and solidification mechanism of magnesium phosphate cement: A review, Constr. Build. Mater. 408 (2023) 133612, https://doi.org/10.1016/j.conbuildmat.2023.133612.
[79] F.C. Serbena, I. Mathias, C.E. Foerster, E.D. Zanotto, Crystallization toughening of a model glass-ceramic, Acta Mater. 86 (2015) 216–228, https://doi.org/10.1016/j.actamat.2014.12.007.
[80] X. Shen, X. Wang, K. Li, X. Hu, C. Shi, Life cycle assessment of magnesium phosphate cement production, J. Clean. Prod. 467 (2024) 142981, https://doi.org/10.1016/j.jclepro.2024.142981.